Tampere University

Aleksi Salmi

ANALYSIS OF HARMONIC CONTENT AND POWER LOSSES OF A FREQUENCY-CONVERTER FED HIGH-SPEED INDUCTION MOTOR SYSTEM

Faculty of Information Technology and Communication Sciences
Master of Science thesis
January 2019

ABSTRACT

ALEKSI SALMI: Analysis of harmonic content and power losses of a frequency-converter fed high-speed induction motor system
Tampere University
Master of Science Thesis, 63 pages, 4 Appendix pages
January 2019
Master's Degree Programme in Electrical Engineering
Major: Power Electronics
Examiners: University Lecturer Jenni Rekola, Assistant Prof. Tuomas Messo

Keywords: filter losses, harmonic content, high-speed vacuum system, power cable configurations, sinusoidal filter

High-speed high-power applications used in vacuum system applications have some unique features compared to other frequency-converter fed motor applications. Operating frequencies and rotational speeds are usually high and significant mechanical stresses occur in rotor. Therefore, solid rotor motors are used due to their mechanical strength. Solid rotor motors are sensitive to supply voltage distortion in terms of eddy current losses and their power factor is relatively low. Therefore, output sinusoidal filters are used at supply converter output. In addition, switching frequencies are relatively low compared to operating frequency. Harmonic contents, sinusoidal filter losses and other relevant vacuum system's supply system characteristics are investigated in this thesis.

Due to low switching frequency and high operating frequency, switching frequency harmonics and base band harmonics might occur at same frequency ranges causing high harmonic amplitudes. Harmonic voltage patterns at different operating frequencies might also be very different. Output voltage harmonics in relevant operating frequencies of Runtech Systems turbo blower application are investigated and analyzed.

Output sinusoidal filter power losses at different operating points are investigated based on measured filter currents. Simplified analytical method to calculate filter power losses is derived based on filter parameters and structure. Due to limited compensation capacity of fixed output filter, filter current distortion is different at different operating frequencies. Therefore, frequency dependency of filter power losses is considered. Different filter structures are used in different vacuum applications. Therefore, filter power loss information is relevant in terms of cooling system design.

Various supply cable configurations and cable lengths are used in different vacuum system field applications. Some power cables are not suitable for certain variable-frequency applications due to their electromagnetic asymmetry. Different power cables are analyzed, and certain cable configurations are suggested for vacuum applications. Purpose of the thesis is to produce valuable information for both product development in future and for vacuum system projects.

TIIVISTELMÄ

ALEKSI SALMI: Suurnopeuskäyttöisen oikosulkumoottorin syöttöjärjestelmän harmonisen sisällön ja tehohäviöiden analysointi
Tampereen yliopisto
Diplomityö, 63 sivua, 4 liitesivua
Tammikuu 2019
Sähkötekniikan diplomi-insinöörin tutkinto-ohjelma
Pääaine: Tehoelektroniikka
Tarkastajat: Yliopistonlehtori Jenni Rekola ja Assistant Prof. Tuomas Messo

Avainsanat: harmoninen sisältö, sinisuodin, suotimen tehohäviöt, suurnopeuskäyttö, syöttökaapelirakenteet

Suurnopeuskäyttöisissä suuritehoisissa alipainejärjestelmissä esiintyy tiettyjä ominaisuuksia, jotka eroavat muista taajuusmuuttajalla syötetyistä moottorikäytöistä. Syöttötaajuudet ja pyörimisnopeudet ovat yleensä korkeita, mikä aiheuttaa merkittävää mekaanista rasitusta roottorille. Monissa sovelluksissa käytetään massiiviroottoreita niiden mekaanisen kestävyyden vuoksi. Massiiviroottorimoottorit ovat pyörrevirtahäviöiden vuoksi herkkiä syöttöjännitteen särölle ja niiden tehokerroin on suhteellisen matala. Tämän vuoksi sinisuotimia käytetään moottoreiden syötöissä. Tämän lisäksi suurtehoisten taajuusmuuttajien kytkentätaajuudet ovat matalia verrattuna suurnopeuskäytön syöttötaajuuteen, mikä aiheuttaa erilaisen harmonisen yliaaltosisällön taajuusmuuttajan jännitteeseen muihin moottorisovelluksiin verrattuna. Tässä työssä tutkitaan suurnopeusmoottorin syöttöjärjestelmän eri osien tehohäviöitä, harmonisia yliaaltoja ja muita tyypillisiä ominaisuuksia.

Matalan kytkentätaajuuden ja korkean syöttötaajuuden vuoksi syöttöjännitteen kytkentätaajuiset komponentit ja perustaajuuden monikerrat saattavat esiintyä samoilla taajuuksilla aiheuttaen korkeita harmonisia komponentteja tietyille taajuuksille. Syöttöjännitteen harmoninen sisältö myös vaihtelee suuresti riippuen käytetystä syöttötaajuudesta. Syöttöjännitteen ja taajuusmuuttajan virran harmonisia sisältöjä analysoidaan syöttötaajuusalueella, jota käytetään Runtech Systemsin alipaineturbosovelluksissa.

Sinisuotimen tehohäviöitä tutkitaan eri toimintapisteissä perustuen mitattuun suotimen virtaan. Työssä muodostetaan yksinkertaistettu analyyttinen malli suotimen tehohäviöiden laskemiseksi. Malli perustuu suotimen ominaisuuksiin ja rakenteeseen. Suotimen rajoitetun kompensointikyvyn vuoksi taajuusmuuttajan virran särön määrä vaihtelee eri toimintapisteissä, minkä vuoksi työssä tutkitaan suodinhäviöiden taajuusriippuvuutta. Koska erilaisia suodinratkaisuja käytetään erilaisissa sovelluksissa, kyky arvioida suodinhäviöiden suuruutta on tärkeää muun muassa jäähdytyksen suunnittelun kannalta.

Erilaisia ja eripituisia moottorin syöttökaapeleita käytetään erilaisissa käytännön alipainejärjestelmissä. Tietyt syöttökaapelirakenteet eivät ole sopivia suuritehoisiin taajuusmuuttajakäyttöihin, koska ne ovat sähkömagneettisesti epäsymmetrisiä. Työssä analysoidaan erilaisia syöttökaapelirakenteita ja käytännön järjestelmiin parhaiten sopivia kaapelirakenteita ehdotetaan. Työn tarkoitus on tuottaa tietoa alipainejärjestelmän syöttöjärjestelmästä sekä tuotekehityskäyttöön tulevaisuudessa että projektikäyttöön erilaisissa ympäristöissä.

PREFACE

This Master of Science thesis was written in co-operation with Runtech Systems by Gardner Denver. I would like to thank everyone who have been supporting and helping me during the project. Special thanks to my supervisor Ville Lahdensuo for giving me so much freedom to choose the research topics according to my interests and to define thesis structure. Thank you also for all other colleagues in Runtech who have helped me during the process. I have learned a lot while working with you.

Moreover, many thanks to my examiners Jenni Rekola and Tuomas Messo in Tampere University for giving valuable feedback during the process and helping me with difficult parts.

Tampere, 16.01.2019

Aleksi Salmi

CONTENTS

LIST OF FIGURES

LIST OF SYMBOLS AND ABBREVIATIONS

A_c	conductor cross-sectional area
A_{core}	core cross-sectional area
AC	alternating current
AFE	active front-end
α	core loss coefficient
B	magnetic flux density
β	core loss coefficient
C	capacitance
C_Δ	delta-connected capacitor
C_Y	star-connected capacitor
c	speed of light
CB-PWM	carrier-based pulse width modulation
D	distortion power
d	core lamination thickness
d_f	inductor foil thickness
d_r	diameter of round conductor
DAQ	data acquisition
DC	direct current
δ	skin depth
Δ	winding loss coefficient
Δ_r	winding loss coefficient for round conductor
DFT	discrete Fourier transform
dv/dt	voltage rate of change
e	Napier's number
E_{core}	core loss density
e_{in}	incoming voltage wave
e_{ref}	reflecting voltage wave
EMI	electromagnetic interference
ϵ_r	relative permittivity
EP-turbo	EcoPump turbo blower
ESR	equivalent series resistance
f	frequency
f_1	fundamental frequency
f_{BB}	harmonic base-band frequencies
f_c	carrier frequency
Δf	frequency resolution
f_g	supply grid frequency
F_m	magnetomotive force
f_{max}	maximum signal bandwidth
f_{mod}	modulating frequency
f_{res}	resonant frequency
f_s	sampling frequency
f_{SB}	harmonic side-band frequencies
f_{sw}	switching frequency
$F(r)$	complex number resulting from discrete Fourier transform
FAT	factory acceptance test
FFT	fast Fourier transform

H	magnetic field strength
I	current root mean square value
I_1	fundamental frequency current
$i(t)$	instantaneous current
I_{active}	active current
I_{dc}	direct current component
I_h	harmonic current component
I_{load}	load current
$I_{reactive}$	reactive current
I_{tot}	total current
IGBT	insulated gate bipolar transistor
j	imaginary unit
J_m	magnetic polarization
k	modulation ration in scalar control
L	inductance
l_{cable}	cable length
l_{core}	core length
L_{dc}	DC-link inductance
L_g	grid side inductance
l_r	length of round conductor
LC-filter	filter consisting inductance and capacitance
m_{core}	core mass
m_f	frequency modulation ratio
μ	permeability
μ_0	permeability of free space
μ_r	relative permeability
N	number of coil turns
$\mathbb{N}$	natural number
N_s	number of samples
NI	National Instruments
P	active power
P_{core}	core power loss
P_{ESR}	capacitor active power loss
$P_{winding}$	winding power loss
PCC	point of common coupling
PE	protective earth
PF	power factor
PF_{tot}	total power factor
ΔP_{filter}	filter power loss
p.u.	per unit
ϕ	phase angle between voltage and current
Φ	magnetic flux
PWM	pulse width modulation
Q	reactive power
Q_c	capacitor reactive power
Q_{load}	reactive power drawn by load
Q_n	nominal reactive power
R_{AC}	AC-resistance
R_{DC}	DC-resistance

R_{ESR}	equivalent series resistance
$\mathfrak{R}$	reluctance
ρ	resistivity
ρ_{core}	core density
RMS	root mean square value
rpm	revolutions per minute, rotation speed
S	apparent power
SVM	space vector modulation
σ	conductivity
σ_{core}	core conductivity
T	period length of periodic signal
t_{rise}	voltage rise time
THD	total harmonic distortion
U	voltage root mean square value
U_c	capacitor voltage
U_{dc}	DC-voltage
U_{inv}	inverter voltage
U_{LL}	line-to-line voltage
U_{phase}	phase voltage
U_s	supply voltage
ΔV_f	filter voltage drop
v_{wave}	voltage wave speed
VFD	variable-frequency drive
X_c	capacitive reactance
Z_{cable}	cable impedance
Z_{dc}	DC-link impedance
Z_f	filter impedance
Z_g	grid side impedance
Z_o	motor boundary impedance
$\mathbb{Z}^+$	positive integer

1. INTRODUCTION

In high-speed high-power applications certain unique phenomena are under interest compared to conventional frequency converter fed induction motor systems. This kind of system is commonly implemented using a large frequency converter and an induction motor with a solid rotor. The solid rotor is preferred due to its ability to withstand stronger mechanical forces which occur in rotors with very high rotational speeds. [1, pp. 18–19] Typical high-speed high-power applications are high-pressure and vacuum systems, where large volumetric flow of gas is required.

Large frequency converters with high current rating are typically relatively slow compared to small power converters due to switching device characteristics and larger currents. This means that maximum allowed switching frequencies remain low or switching losses increase intolerable high if switching frequency is increased. [2, pp. 627–630] Low switching frequency combined with high operating or supply frequency of the motor might create very different voltage and current harmonic pattern compared to low-speed or low-power applications.

Frequency converters or variable-frequency drives naturally create pulsating output voltage waveform due to their switching operation. To guarantee proper operation of the high-speed solid rotor motor, output filter is required to mitigate output voltage distortion. A solid rotor motor is especially sensitive to supply voltage distortion in terms of rotor losses. [1, p. 86] In addition, high-speed motor is also sensitive to overvoltage spikes, because strengthened stator winding insulation cannot be used due to limited space. Therefore, use of proper output filter is critical for proper motor operation. As a tradeoff, output filter increases system power losses and decreases effective voltage due to voltage drop over filter.

Purpose of this thesis is to investigate power losses and voltage and current harmonics at different segments of supply system of the EcoPump turbo blower. EcoPump (EP) products are turbo blower products made by Runtech Systems by Gardner Denver. EP-turbo products can be used to create high vacuums for different purposes in paper and pulp industry. Power range of EcoPump products is up to 600 kW and they can achieve rotational speeds over 10000 rpm. EP turbos are supplied by variable-frequency drives (VFD) to achieve large speed range without mechanical gears.

Under special interest are the output sinusoidal filter, supply voltage harmonics and supply cable considerations. Filter power losses seem to vary significantly at different operating points and therefore the filter loss behavior is investigated carefully. VFD output

voltage and current harmonics and effects of the output filter are investigated by measurements and theoretical analysis to better understand sources of different harmonic components at different operating points. Supply cables are considered to produce useful information for practical field applications. Analysis of system losses and harmonic contents are combination of measurement data from the actual EP-turbo supply system and theoretical electromagnetic analysis and calculations. EP turbo blower structure, motor design and detailed analysis of the variable-frequency drive structure are left out of the thesis scope and they are considered only in general level.

Structure of the thesis follows the structure of the supply system from the supply grid to motor terminals. EP turbo blower, a solid rotor motor, supply system structure and used measurement setup are presented in Chapter 2. Chapter 3 includes analysis of the variable-frequency drive containing both input and output voltage and current analysis at different operating points. Most attention is paid to VFD output waveforms and harmonic analysis. Output filter structure, loss analysis, voltage drop behavior and reactive power compensation analysis are presented in Chapter 4. Filter losses are calculated based on filter current measurement and theoretical analysis of filter structure and power loss mechanisms. Chapter 5 concentrates on motor supply cables and motor terminal voltage characteristics from practical, field application-based perspective. Chapter 6 is a conclusion summarizing most relevant results and investigations.

All in all, main goal of the thesis is to get more information and better knowledge of the vacuum system's supply system losses and behavior of the supply harmonics. Furthermore, this information could hopefully be used to improve product efficiency and reliability in the future. Understanding of the output filter loss mechanisms and filter's capability to mitigate voltage and current distortion at each operating point are particularly interesting because of importance of the filter. Multiple different VFDs and output filters are used in different field installations all over the world and ability to evaluate losses of different filters is important.

2. SYSTEM DESCRIPTION

2.1 EcoPump turbo blower

Runtech EcoPump -products are high-speed turbo blowers which are used to create high vacuums for paper and pulp industry. They are used especially in paper machine forming section and press section. In the forming section, vacuum is used to dewater the paper stock and in press section, vacuum is used to dewater and clean the press felts. Very often EcoPumps are used together with RunDry suction boxes, EcoDrop water separators and EcoFlow dewatering measurement systems. EcoPumps are one- or two-stage turbo blowers with composite or titanium impellers. EP-turbo blowers are completely water-free variable speed blowers. [3, 4] Example of EP600-S turbo blower is shown in Figure 1.

Figure 1. *Two-stage EP600 turbo blower [3].*

EcoPumps' rated powers are 315–600 kW, maximum vacuums are -10– -70 kPa and they weight 3500–5000 kg. Most EPs consist high speed solid-rotor induction machine with a single pole pair and ceramic ball bearings. Nominal operating frequencies are either 160 Hz or 170 Hz depending on EP model. Maximum rotation speed of the smaller 315 kW EP315 turbo is up to 10200 rpm [5]. As an example, general data of the two-stage EP600-S shown in Figure 1 is presented in Table 1.

Table 1. *General data of EP600 turbo [3].*

Max. vacuum	Max. air flow	Rated power	Supply voltage
−70 kPa	8.5 m^3/s	600 kW	400/690 V
Weight	Size (L x H x W)	Max. speed	Impeller
5000 kg	2.62 x 2.25 x 1.72 m	9600 rpm	Titanium or composite

EcoPumps are fed by variable-frequency drives (VFD) to achieve wide operation range without mechanical gears. Motor coils are connected in delta or star configuration depending on customer's supply voltage level. Impellers are attached directly to the motor shaft. To generate adequately sinusoidal supply voltage waveform and to compensate reactive power drawn by the induction motor, a sinusoidal filter is connected to VFD output terminals.

In most applications EP-turbos run at constant speed near the nominal speed most of the time. Depending on required vacuum levels, vacuum system structure and customer's needs, turbos might also be used at lower speeds such as 8400 rpm (140 Hz) or 7200 rpm (120 Hz). Turbos are very often used in harsh industrial environment where humidity, dust and other dirt might cause challenges and that's why reliable and robust operation of the motor is essential.

2.2 Solid rotor motor

A solid rotor motor is an induction motor whose rotor is made of single piece of steel. Compared to laminated rotor, solid rotor is mechanically stronger and more stable due to the single-piece structure. For this reason, it is especially suitable for high-speed applications, where centrifugal forces and mechanical stresses are strong and conventional laminated rotor would not be strong enough. This is also the case with EP-turbos where tangential speed of the rotor edge is extremely high. General structure of the rotor is simple, because stacking structure or steel sheet attachment don't need to be considered. [1, pp. 18–24]

From the electromagnetic perspective, a solid rotor motor is not the most straightforward solution. In traditional squirrel-cage induction machines electric and magnetic circuits can be quite accurately considered as separate circuits. Cage forms the electric circuit and rotor core and air-gap the magnetic circuit. In the solid rotor machine this is not the case, which makes analysis more complicated. Magnetizing current in rotor flows in the solid rotor core, which is also the path of the magnetic flux. This makes rotor calculation very complicated and non-linearity of the core material must be taken into account also in electric circuit calculation. [1, pp. 31–32]

Due to the magnetic non-linearity and common path of rotor current and magnetic flux, solid rotor is seen as highly inductive load from a stator perspective. Power factor of the solid rotor induction machine is much lower compared to the regular laminated induction motor. For the same reasons, rotor slip is relatively high. Power factor of the solid rotor motor is generally between 0.65–0.75 while power factor of the conventional laminated squirrel-cage machine at same kind of power characteristics can be as high as 0.90. [1, pp. 102–103]

Main reason for regular rotor lamination is to mitigate eddy currents induced by air-gap flux. Due to lamination, eddy currents flow at narrow sheets and eddy-current resistance is high. In solid rotor, rotor is made of single piece and eddy currents experience low resistance paths. As a result, ohmic losses caused by eddy currents might be much higher compared to the laminated rotor motor of same power rating. The solid rotor is also particularly sensitive to deviation of the air-gap flux. If the air-gap flux differs from sinusoidal, eddy current losses of the rotor could be significantly higher compared to ideal sinusoidal flux. In the solid rotor motor, different losses caused by the magnetic flux and current harmonics can be more than 10 % of the total losses while same percentage is only couple per cents in the laminated rotor motor. [1, pp. 62–63] For this reason, motor supply voltage waveform should be as sinusoidal as possible.

Eddy current losses and solid rotor motor performance can be improved by different structural arrangements. Adding axially directed slits to a rotor surface, the magnetic flux penetrates deeper into the rotor and eddy currents are forced to flow paths of higher impedance. Rotor slits reduce eddy current losses and decrease rotor slip. [1, pp. 47–48] Performance of the solid rotor can also be improved with end rings made of low-resistance material, such as copper. End rings make currents flow nearly axial direction and improve rotor torque production. [1, pp.49–52]. Example of possible solid rotor structure with slits and end rings is shown in Figure 2.

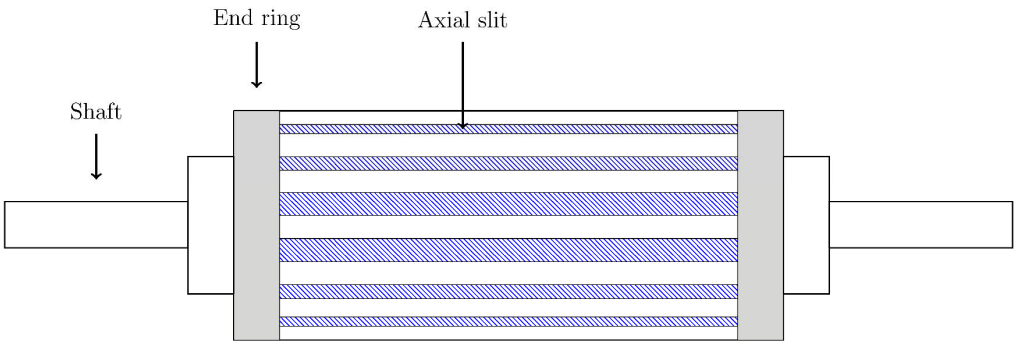

Figure 2. *Example of solid rotor with slits and end rings. Based on [1, p. 25].*

Unlike solid steel rotors, EP-turbo motor stators are electromagnetically quite simple. Due to motor dimensions, limited space and thermal behavior, each stator winding consists of only one winding turn. This makes the stator conceptually simple because winding

structure doesn't have to be considered. In addition, proximity effect and couplings between winding turns don't exist. On the other hand, all the electrical stress in stator winding is focused on to the same winding turn, which causes stress to winding insulation. Due to limited space of the stator winding, reinforced or extra strong winding insulation cannot be used. As a result, stator winding is sensitive to extra voltage stress and high voltage spikes. Too high repeating voltage spikes might in worst case cause system failure.

2.3 Factory acceptance test setup

As described in Chapter 2.1, EP turbo blowers' induction motors are fed by variable frequency drive. In Runtech's factory acceptance test (FAT) setup in Kotka, Finland, ABB ACS880 drive is used. Drive system rectifier side consist of two parallel rectifier modules which behave as six-pulse rectifiers. Inverter side consists of three parallel-connected insulated gate bipolar transistor (IGBT) -based inverter modules.

Drive system is fed by an autotransformer, which transforms 400 V supply grid line voltage to 690 V. The autotransformer is a supply transformer with only one common winding without galvanic separation between primary and secondary sides. This makes the autotransformer smaller and less expensive compared to a conventional supply transformer with separated primary and secondary. The use of a transformer makes it possible to test turbos at same voltage level and motor connection in which they are used in the field. A sine wave filter is connected between motor and drive system output terminals to re-shape output voltage waveform to be more sinusoidal and to compensate the motor magnetizing current. General structure of the FAT-setup supply system with delta-connected motor is presented in Figure 3.

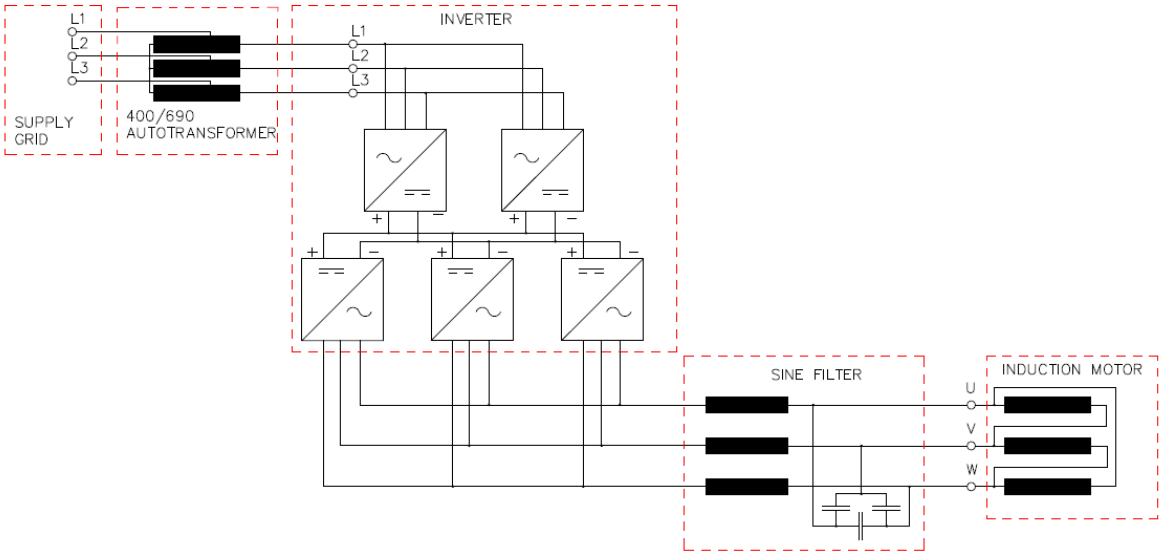

Figure 3. *Induction motor supply system in FAT-setup.*

Different customers have very different supply systems and structure of the VFD system can differ from Figure 3. In real field applications VFD is usually supplied by common supply transformer of the paper factory and separate autotransformer is not used. Different customers might use products from different VFD and filter manufacturers, but general structure remains the same. Very often there are also multiple EP-turbos working simultaneously and these are fed by separate VFDs but from the same supply transformer.

The sine filter plays an important role for proper functioning of the motor and the whole supply system and it is usually physically integrated to VFD chassis. To ensure proper filter operation, separate filter cooler is attached to filter chassis. Different filter structures can be used, and filter capacitors can be connected either star or delta depending on supply voltage level. In the FAT-setup, VFD is connected to the turbo via 1x185 single conductor copper conductors and two conductors per phase are used. In the FAT-configuration the distance between the VFD and turbo test bunker is less than 10 m, so the supply conductors are quite short. In real paper industry applications supply cable configuration might be very different and multiple different supply cable structures might be preferred. Distance between the supply and the motor can also be much longer.

2.4 Measurement setup

To better investigate current and voltage behavior at different parts of the turbo supply system, new power analyzer with higher bandwidth was acquired. All voltage and current measurements in this thesis are carried out using portable power analyzer made by Kurelco Oy. Analyzer is based on National Instruments' (NI) products consisting N19171 rack and 16-bit NI9220 data acquisition tool (DAQ). Power analyzer has six parallel channels which makes it possible to measure two three-phase systems simultaneously. Power analyzer is connected to a Windows PC via USB-port and the system is operated using NI LabVIEW software.

Voltage measurements are implemented using high-bandwidth Hall-effect based LEM CV3-2000 voltage transducers. Currents are measured using Fluke i3000s current clamps. Fluke's current clamps are Rogowski-coils where voltage proportional to the current derivative is induced to clamp. After data processing i.e. integration, current value at each time instant can be calculated. Due to the working principle of the current probes, they are very fast but quite sensitive to external magnetic fields and disturbances. This must be considered while currents are measured near filter inductors, where external magnetic field could disturb the measurement. During measurements current clamp cables should not be too close to the inductor coils. Example of the measurement setup during filter voltage and current measurement is show in Figure 4.

Figure 4. *Measurement setup.*

Fluke current probes have bandwidth of 20 kHz [6] while the voltage transducers have bandwidth up to 300 kHz [7]. The measurement system enables maximum sampling frequency of 100 kHz and input voltage range ±10 V [8]. In 16-bit system 20 V voltage range means that theoretical voltage resolution of the measurement is approx. 0.3 mV. According to the Nyquist sampling theorem, theoretical maximum value of the signal bandwidth for accurate measurements and frequency analysis is

$$f_{max} \leq \frac{1}{2} f_s, \tag{1}$$

where f_{max} is maximum signal bandwidth and f_s is sampling frequency of the measurement system [9, p. 545]. Based on (1), 100 kHz sample frequency gives accurate measurements up to 50 kHz. In reality, bandwidth of current probes is below that. Since both filter and motor inductances damp current oscillation and limit rate of change of the current, very rapid current changes should not occur. Based on that, current measurements should be accurate enough even though analyzer scanning frequency is higher than current probe bandwidth. On the other hand, VFD output voltage is highly pulsating containing some very short pulses. Due to this, shortest switching pulses might not be measured accurately, which could cause error to the voltage measurements before output filter. Output filter mitigates voltage variation substantially and the voltage measurements after the filter should be accurate enough.

3. VARIABLE-FREQUENCY DRIVE

3.1 Mathematical background

According to the Fourier's theorem, any repeating sinusoidal or non-sinusoidal waveform can be expressed as a sum of different sinusoidal components with different frequencies and phase shifts. Any non-sinusoidal current can be expressed as

$$i(t) = I_{dc} + i_1(t) + \sum_{h=2}^{\infty} i_h(t), \tag{2}$$

where $i(t)$ is non-sinusoidal repeating current waveform, I_{dc} is DC-current component (bias), $i_1(\mathrm{t})$ is the current component at fundamental frequency and $i_h(t)$ is so called harmonic current component [2, pp. 39–40]. Sum of the harmonic current components can be called distortion current. In addition to current, (2) can be obtained to voltage or any other repetitive time-domain signal.

Root-mean-square -value (RMS-value) of the periodic current can be calculated

$$I = \sqrt{\frac{1}{T}\int_0^T i(t)^2 dt}\,, \tag{3}$$

where T is period of the current [2, p. 34]. Again, same analysis can be obtained to any other periodic continuous signal. The amount of current distortion can be evaluated using total harmonic distortion (THD)

$$\%THD = 100 \cdot \frac{\sqrt{I^2 - I_1^2}}{I_1}, \tag{4}$$

where I is RMS-value of the whole current and I_1 is RMS-value of the fundamental current component [2, p. 42]. If the waveform is close to sinusoidal or doesn't include significant high order harmonics, (4) can be simplified by calculating nominator by square-summing up only harmonic amplitudes up to some limit. Common practice is to consider harmonics up to 40$^{\text{th}}$ harmonic component and it is based on European power quality standards [10].

To use THD or other similar frequency component-based analysis tools, efficient way to divide time domain signals to different frequency components according to (2) is needed. When sampled measurement data is analyzed, discrete Fourier transform (DFT) can be used to present discrete time domain signal in frequency domain. DFT presents the fre-

quency content of the signal i.e. how much time-domain signal consists different frequencies. Content of certain frequency of time discrete data of N samples is analytically defined as

$$F(r) = \sum_{n=0}^{N-1} f(n) \left[\cos\left(\frac{2\pi}{N_s}\right) - j \sin\left(\frac{2\pi}{N_s}\right) \right]^{nr} \quad (5)$$

where $F(r)$ is complex number presenting content at certain frequency and j is an imaginary unit [11, p. 9]. DFT divides frequency range to equally spaced frequency components and frequency ratio is defined by sampling frequency and number of datapoints as

$$\Delta f = \frac{f_s}{N_s}. \quad (6)$$

For example, 1 s measurement sequence at 100 kHz sampling frequency equals 100 000 samples which again according to (6) gives frequency ratio of 1 Hz. Again, according to Nyquist theorem, only frequencies below half of the sampling frequency are relevant and DFT output starts to repeat itself after frequencies above $\frac{1}{2} f_s$.

DFT can be efficiently computed using algorithm called Fast Fourier transform (FFT) [11, pp. 9–10]. Many commercial software such as Microsoft Excel or MATLAB provide build-in tools and FFT-algorithms to calculate DFTs of measurement data. Depending on the software, FFT-algorithms return complex number in some format, which again can be separated to amplitude and phase angle information. Corresponding frequencies can then be calculated by dividing sample frequency equally spaced frequency sequence starting from zero frequency. Finally, nth component in FFT-output array corresponds to nth component in frequency-sequence array.

Power drawn by a motor or other load can be described with power factor (PF)

$$PF = \frac{P}{S} = \frac{UI \cos(\phi)}{UI} = \cos(\phi) \quad (7)$$

where P is active power, S is apparent power, I is phase current, U is phase voltage and ϕ is phase-angle between current and voltage [2, p. 36]. Phase-angle version of (7) can be used if both current and voltage are sinusoidal. Power factor can be used for total power or by component-wise using currents and voltages at different frequencies.

So-called reactive power Q describes non-active part of the apparent power. For sinusoidal quantities, reactive power at certain frequency can be defined as [2, p. 36]

$$Q = UI \sin(\phi). \quad (8)$$

Reactive power is not realized as other form like heat or active work. Instead, reactive power describes the amount of energy that is stored to or released from electromagnetic fields of the system.

For non-sinusoidal waveforms, total power factor can be calculated by

$$PF_{tot} = \frac{I_1 \cos(\phi_1)}{I_{tot}} \tag{9}$$

where I_1 and I_{tot} are fundamental and total current RMS-values [2, p. 43]. Total current RMS can also be divided into different component as

$$I_{tot} = \sqrt{I_{active}^2 + I_{reactive}^2 + I_{harmonic}^2} \tag{10}$$

where I_{active} is sinusoidal active current, $I_{reactive}$ is sinusoidal reactive current at 90° phase-shift with active current and $I_{harmonic}$ is non-sinusoidal harmonic current component [12]. Similarly, total apparent power can be expressed as a square-sum of the power components as

$$S = \sqrt{P^2 + Q^2 + D^2} \tag{11}$$

where D is so called distortion power taking into account non-sinusoidal part of the total power distribution [12].

As seen from (10), if the load current is non-sinusoidal, total current is larger compared to the purely sinusoidal current. On the other hand, if load draws some reactive current, total current increases. As a conclusion, both reactive power demand and non-sinusoidal current behavior increase the total current. In general, higher total current implies higher power losses and components with larger current rating, which usually are more expensive. Some loads naturally demand reactive power, so unity power factor can't be achieved. However, reactive power can be at least partly produced by power filter connected between supply and load. Reactive power can be then produced near load, and supply current can be decreased. In other words, power factor seen by supply terminals becomes closer to unity. Efficient reactive power compensation can decrease total current drawn from supply significantly. In some cases, it enables use of smaller VFD which usually means significant cost reduction.

3.2 VFD supply, rectifier and DC-link

Generally, variable-frequency drive consists of rectifier, DC-link, inverter, control system and auxiliaries. Larger VFDs with high current rating consist of multiple parallel rectifier and inverter modules. Diode-based rectifier can be either passive (only power diodes),

half-controlled (each leg consists one diode and one thyristor) or controlled (only thyristors). Generic three-phase VFD-schematic with half-controlled six-pulse rectifier with diodes and thyristors, DC-link capacitor and IGBT-based inverter with antiparallel diodes is shown in Figure 5. VFD in Runtech's FAT-setup is based on that kind on rectifier and inverter modules.

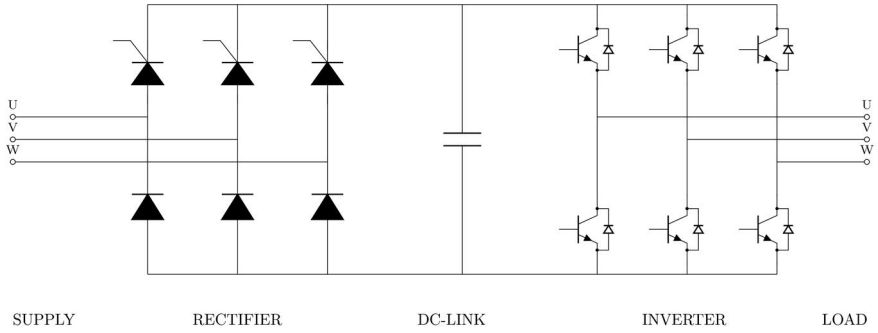

Figure 5. *Generic VFD schematic.*

In addition to diode-based rectifiers, rectifier side can also be implemented with active switching components. This kind of arrangement is called active front end (AFE). [13] AFE enables possibility to transfer power both directions and it can be used to feed power to the supply grid. AFEs are used in so called low-harmonic VFDs, because they can be operated in a way that harmonics caused to the supply point are minimized and the supply current is basically sinusoidal.

Three-phase diode or thyristor rectifier is called six-pulse rectifier due to its output voltage waveform. In a half-controlled rectifier, firing angles of the thyristors in upper half-legs can be controlled and DC-link voltage can be increased slowly during start-up conditions. By doing so, large inrush current spikes can be avoided. To achieve maximum DC-link voltage during normal operation, firing angles are set to be zero and thyristors behave as diodes. [2, pp. 149–156]

In the case of ideal three-phase rectifier and nominal operation, DC-voltage is pulsating at the frequency of six times the supply voltage fundamental frequency. DC-link capacitor or capacitors regulate rectifier's output voltage and reduce voltage pulsation. In diode operation, rectified DC-voltage can be calculated by integrating supply line-to-line voltage over one pulse i.e. over 1/6 of the full period. Ideally, the average DC-voltage is

$$U_{DC,ave} = \frac{3\sqrt{2}U_{LL}}{\pi}, \tag{12}$$

where $U_{DC,ave}$ is the average DC-voltage and U_{LL} is supply line-to-line voltage [14, p. 139]. In real life applications, DC-voltage is never that high due to non-ideal components,

non-zero rectifier inductance and component losses. In addition, input inductance is very often added to VFD's input terminals to reshape input current waveforms and to limit rate of change of the current.

If a six-pulse rectifier operates in diode mode, each diode conducts only 1/3 of the period at the time. If inductance of the rectifier would be zero, current would rise and fall immediately, and phase current would be square-shaped at 1/3 of the period. Example of line current and supply line voltage waveforms in ideal case with zero inductance are shown in Figure 6. In Figure 6, current rises and falls immediately.

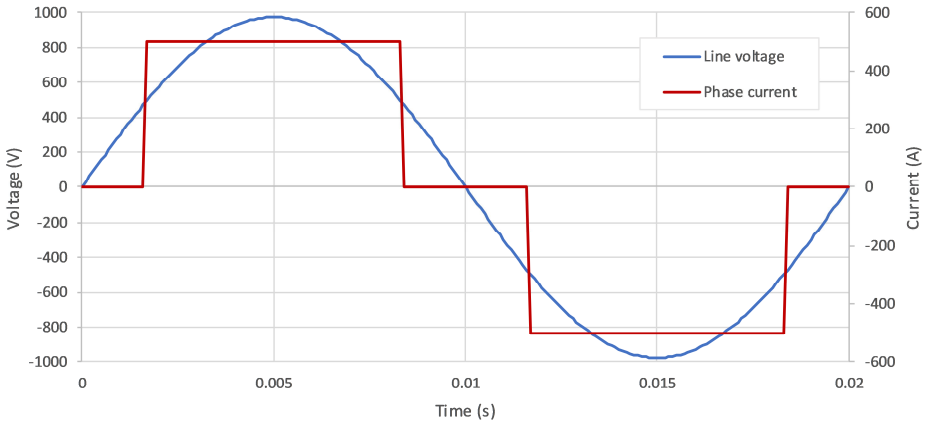

Figure 6. *Example of line current waveform with zero inductance.*

In literature [2, pp. 104–106, 15], the harmonic analysis of the rectifier current is based on Fourier-analysis of square-shaped current waveform, which refers to constant DC-side current. Based on this analysis, harmonics of the rectifier current can be calculated. Harmonic current RMS-values are

$$I_h = \frac{1}{h} I_1, \tag{13}$$

where I_h is RMS-value of h^{th} harmonic component, I_1 is amplitude of fundamental current component and h is the order of the harmonic component [2, p. 105]. In three-phase rectifier, current harmonics occur at frequencies according to $h = 6k \pm 1,\ k \in \mathbb{N}$ [2, p. 86]. This means that only odd non-triplen (not dividable by three) harmonics occur in current waveform. Analysis above leads to high 5^{th} and 7^{th} harmonic current components and calculated THD up to 40^{th} harmonic is 29.68 %.

Analysis above assumes perfectly flat and square-shaped current waveform. Due to system inductance, current rise time is not zero. In the middle of the current pulse in Figure 6 current changes from one diode to another and this shift takes finite time. It implies that there is a short time period when both diodes are conducting. This phenomenon is called current commutation. Current commutation decreases rectifier output voltage and causes two pulses to current waveform in each conducting period. [2, pp. 109–111]

Current commutation leads to harmonic RMS-values slightly different than (13) implies. Each pulse includes two peaks which means that 5th harmonic component is significantly higher than (13) implies. On the contrary, all the higher-order harmonics are much lower than (13) indicates. [15] Different harmonic amplitudes mean that also current THD is different than calculated value above. Reduction of higher order harmonics probably cause lower THD value even though amplitude of the lowest harmonic is higher.

VFD rectifier current and voltage characteristics of the 400/690 V supply autotransformer of the FAT-setup were investigated. Transformer secondary phase voltages and currents were measured with and without the load. At load test, average power of 500 kW and average RMS-current of 450 A were drawn from the autotransformer. Secondary side phase voltage and current of loaded transformer are shown in Figure 7.

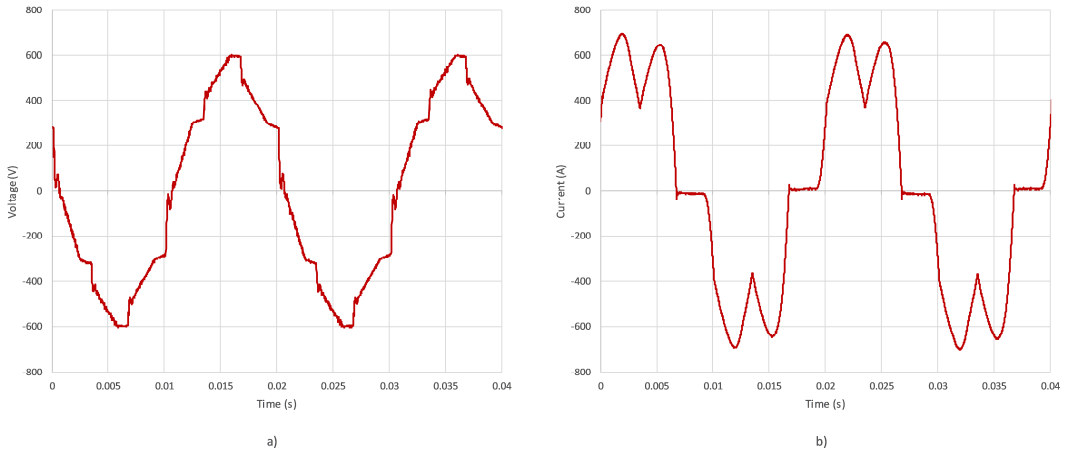

Figure 7. *Supply autotransformer secondary quantities at 500 kW. a) Phase voltage b) Current.*

As seen in Figure 7, current drawn by VFD is significantly distorted and current waveform is very different compared to Figure 6. This is due to rectifier inductances and current commutation. Current commutation can also be seen from the voltage waveform, where small notches are seen at every 1/6 of the period. These notches are caused by the commutation voltage which occurs due to inductance and commutation current. [2, pp. 107–108] In addition to current commutation, distorted current causes distortion to the supply voltage via transformer and cable impedances.

If other equipment would be connected to the same supply, distorted voltage could possibly cause some undesired phenomena or even malfunctioning of the equipment. In autotransformer, lack of galvanic separation causes that distorted secondary voltage causes significant distortion also to the primary side. If regular supply transformer would be used, galvanic separation and transformer inductance would damp at least higher order voltage harmonics and decrease distortion effects in primary side voltage.

Figure 8 presents normalized harmonic spectra of transformer secondary phase voltage and current. Normalized spectrum means that amplitude of fundamental frequency component is scaled to be one or 100 %. Spectra are calculated from measured data with discrete Fourier transformation and FFT-algorithm. As indicated in (13), rectifier current consists significant non-triplen odd harmonics. In current spectrum, amplitude of 5th harmonic is 27 % which is higher that (13) predicts (20 %). On the contrary, amplitude of 7th harmonic is only 6 % which is much less than square-current analysis assumes (14.3 %). In addition to predicted non-triplen harmonics, current spectrum consists 3rd harmonic with small amplitude (2 %).

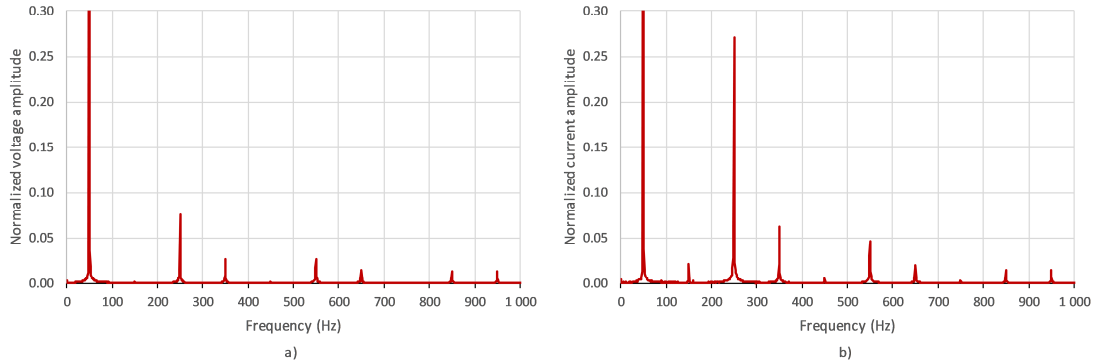

Figure 8. *Normalized harmonic spectra of transformer secondary. a) Phase voltage spectrum b) Current spectrum.*

Transformer loading has significant effect on supply voltage THD. Calculated phase voltage THD up to 40th harmonic was 0.72 % at no-load conditions, which means that voltage was almost perfectly sinusoidal. When average power of 500 kW was drawn, secondary voltage THD was increased to 8.62 %. Almost all the same harmonics that occur in current spectrum are also seen in voltage spectrum but with much lower amplitudes. At the same time, current THD under 500 kW load was 28.36 % which is very close to square-shaped current THD (29.68 %) calculated based on (13). Harmonic amplitudes are different when rectifier inductance occurs, but total THDs seem to be almost equal.

At every instant, two phases are connected to DC-link via diodes. This circuit can be modelled as an equivalent impedance model shown in Figure 9, where Z_g represents a combination of grid impedance per phase and possible input choke and Z_{dc} is impedance of DC-link per phase.

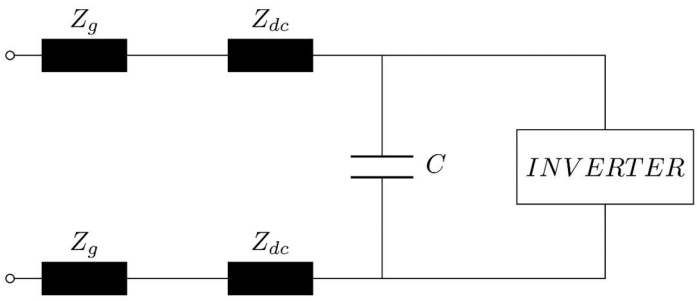

Figure 9. *Equivalent impedance model of rectifier side. Based on [16, 17].*

Inductances of impedances Z_g and Z_{dc} and capacitance C in Figure 9 form a series resonant circuit. Resonant frequency at certain time instant can be calculated

$$f_{res} = \frac{1}{2\pi\sqrt{2(L_g + L_{dc})C}}, \tag{14}$$

where L_g and L_{dc} are inductances of grid and DC-link correspondingly [16]. As seen from (14), resonant frequency of the rectifier circuit doesn't depend on load characteristic. If VFD includes multiple rectifier modules or multiple drive systems are connected to same point of common coupling (PCC), impedance and resonance characteristics seen from PCC differs from single drive connection. As a number of parallel drives increases, total impedance seen from PCC decreases and resonant frequency decreases accordingly. If all drives are equal, resonant frequency between supply impedance and DC-links decreases by factor of $\frac{1}{\sqrt{n}}$, where n is number of equal parallel drive systems. Lower resonant frequency might cause undesired phenomena, if resonant frequency becomes very close to operating frequency. If one or couple drive units are connected to PCC, system could operate properly. Resonance problems might occur, when number of units is increased. [16]

According to [17], inverter side harmonic emissions to supply side can be mitigated by selecting resonant frequency at least 6 times higher than supply grid frequency. In addition, rectifier resonant frequency should be less than inverter switching frequency. This relation can be defined

$$6f_g < f_{res} < f_{sw}, \tag{15}$$

where f_g is supply grid frequency and f_{sw} inverter switching frequency [17]. (15) can be used to set limits to either value of DC-link capacitor or grid side inductances. For regular 50 Hz grid supply, (15) gives 300 Hz lower limit for resonant frequency. For fixed DC-capacitor value, too small inductance values might increase resonant frequency too high and vice versa. In practical applications, too long supply cables could possibly increase

rectifier input impedance too high, which again could decrease resonant frequency below the lower limit of (15).

Analysis above concentrates on low-order (below 2 kHz) harmonics caused by the diode rectifier. At the case of 50 Hz supply, 2 kHz corresponds to 40^{th} harmonic component. Rectifier side harmonics at frequencies above 2 kHz are analyzed in [16]. Generally, high-frequency rectifier harmonics are attenuated effectively by DC-capacitor and DC-link inductance and they should not be drifted to supply side. Based on VFD supply measurements, inverter switching frequency harmonics and other higher harmonics cannot be seen in the supply side.

3.3 VFD output control

Basic principle of the motor control is to produce high rotor speed values without rotor speed measurements. Absolute accuracy of rotor speed and rotor torque control are not required because main goal is to produce high volumetric air flows and vacuums at certain operating points. For this reason, so called scalar control is used. In scalar control (U/f-control), ratio of the motor supply voltage reference and operating frequency is kept constant. Scalar control is conceptually very simple control method, because it is based on motor steady-state parameters. The tradeoff is that fast and accurate responses to stepwise changes to reference or disturbances can't be achieved. [18, pp. 401–403] In EP-turbo drives this doesn't matter because fast reference changes will not occur under normal operating conditions, and rotor speed reference is kept constant or changed with slow ramps.

To investigate the relation of operating frequency and supply voltage, motor supply line-to-line voltage was measured at different supply frequency references between 60–160 Hz. RMS-values of total line voltage and fundamental voltage components at each operating point are shown in Figure 10.

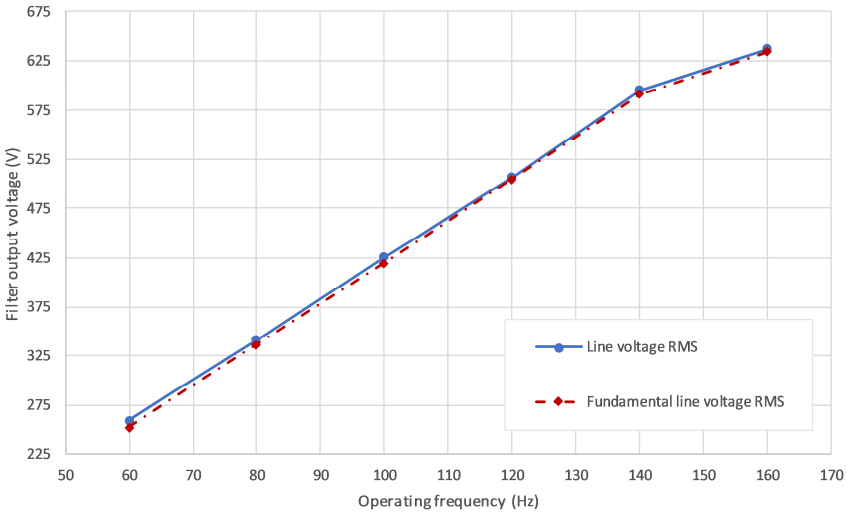

Figure 10. *Filter output line voltage and fundamental component at 690 V supply.*

As seen from Figure 10, supply voltage increases linearly from 60 to 140 Hz. U/f-ratio of line voltage is approx. 4.2. After 140 Hz voltage doesn't increase linearly anymore and U/f-ratio doesn't remain constant. This is due to overmodulation region where some of the reference pulses are ignored, and voltage control is not completely linear any more.

Depending on the modulation technique, theoretical maximum value of inverter output line voltage is either $\frac{1}{2}\sqrt{\frac{3}{2}}U_{dc} \approx 0.61U_{dc}$ conventional pulse width modulation (PWM) or $\frac{1}{\sqrt{2}}U_{dc} \approx 0.71U_{dc}$ in 3rd harmonic injected PWM, space-vector modulation (SVM) etc. [19, p. 349]. As stated in (12), theoretical maximum of DC-link voltage without capacitor regulation is approx. $1.35U_{s,LL}$. This means that even if extended linear modulation range is used, maximum inverter output fundamental voltage is

$$U_{inv,LL,max} = \frac{3}{\pi}U_{s,LL} \approx 0.95U_{s,LL.} \tag{16}$$

(16) implies that even theoretically inverter output line voltage cannot be as high as supply line voltage in linear modulation region. In real applications, non-ideal components and voltage notching decrease effective output voltage as described in Chapter 3.2. To achieve maximum output voltage, linear region must be extended, and linear U/f-ratio is violated. In addition to non-linear control, operating in overmodulation region includes another drawback. Overmodulation affects voltage harmonics by increasing amplitudes of both baseband and side-band harmonics. [19, pp. 354–355]

In very low frequencies, resistive voltage drop over stator winding could become dominant compared to total output voltage. This causes that effective output supply voltage becomes lower than expected and constant U/f-ratio doesn't produce desired effective voltage. Voltage drop at low frequencies can be taken into account by modifying U/f-

ratio if operating frequency is very low. This modification is called IR-compensation. [18, p. 402] In EP-turbo applications operating frequency is never very low in normal operation region and if low frequency is used, accurate supply voltage value is not relevant. This makes it possible to ignore IR-compensation, which makes U/f-control even more simple.

3.4 Inverter and modulation

General principle of carrier-based pulse width modulation (CB-PWM) is to compare carrier signal and modulation signal and generate inverter switching commands accordingly. There are numerous different CB-PWM-techniques and different modulation and carrier signals for different applications. Conceptually most simple three-phase CB-PWM-technique is sinusoidal triangle-wave PWM, where sinusoidal modulation signal is compared to triangle-shaped carrier signal. In sinusoidal CB-PWM, inverter switching frequency is determined by carrier signal frequency in linear modulation range. Modulation signal frequency determines fundamental frequency of the output voltage.

In addition to the sinusoidal CB-PWM, there are more sophisticated ways to implement modulation signals, such as space-vector modulation (SVM). In addition to conventional modulations with sinusoidal references, one widely used variation of general sinusoidal CB-PWM is so called bus-clamping modulation.

3.4.1 Bus-clamping modulation

Main idea of bus-clamping modulation (or discontinuous modulation) is to reduce average switching frequency without significantly affecting harmonic content of three-phase output voltage. In other words, with same average switching frequency, bus-clamping modulation produces lower voltage harmonic content compared to conventional CB-PWM or SVM. [20] In high power applications even a small reduction of switching events can decrease total switching power losses significantly.

In general, in bus-clamping modulation one phase is connected to positive or negative DC-link rail continuously 1/3 at one half-cycle i.e. connected to DC-link 1/3 of the full cycle. Modulation signal is generated in a way that one phase is connected to either positive or negative DC-rail at every time instant. Bus-clamping modulation signal can be produced various ways, for example by injecting a common-mode signal to sinusoidal modulation signals. Common-mode signal can be generated by choosing largest and smallest sinusoidal modulation signal at every instant and substituting signals from 1 or -1 correspondingly. Then, one of the two common mode signal components is chosen according to reference pulse signal. In addition to common mode injection, bus-clamping modulation signals can be generated by using modified SVM-based switching commands (advanced space vector modulation). [20, 21]

If common-mode signal method is considered, generated common-mode signal must have period of $3n, n \in \mathbb{N}$ times modulating signal period. Resulting modulating signal can be modified by adjusting delay angle of the common-mode signal i.e. first zero-crossing time of the common-mode signal. Delay angle can be shifted between 0-60˚ of modulating signal period (0-180˚ of common-mode signal's own period). Adjusting modulation index i.e. amplitude of sinusoidal modulation signal has no effect on clamping period or the time instant when clamping occurs.

Examples of different bus-clamping modulating signals and corresponding switching commands for upper switch of phase A are shown in Figure 11. In Figure 11, fundamental frequency is 160 Hz and carrier frequency 3.5 kHz.

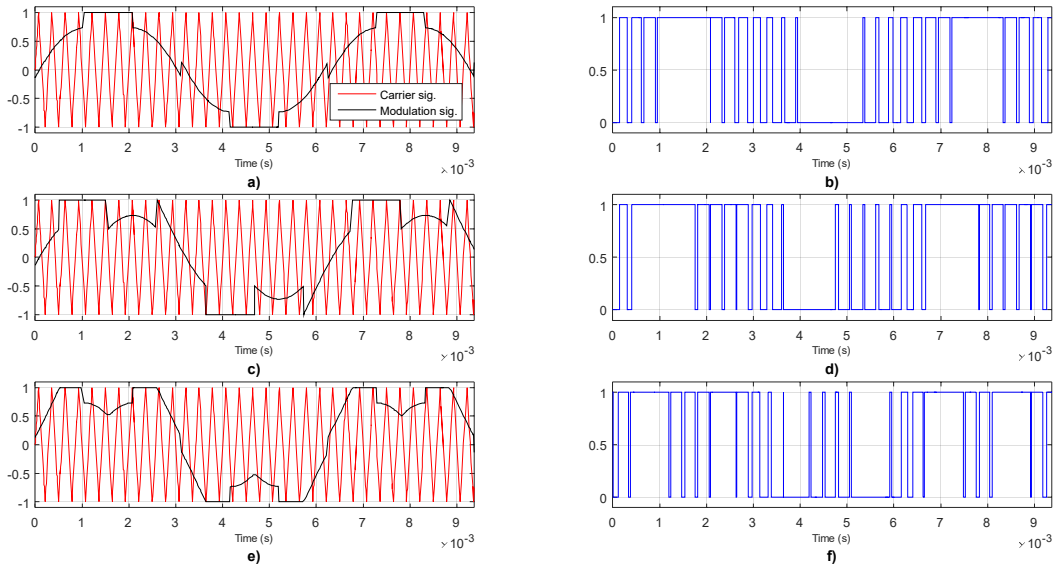

Figure 11. *Bus-clamping modulating signals and corresponding switching commands. Based on [20].*

In Figure 11, a) is called 60˚ clamping and it corresponds to reference signal delay angle 60˚. Inverter phase leg is clamped 60˚ at the time and clamping occurs around the peak of sinusoidal signal. 60˚ clamping is most preferred for resistive loads, because both current and voltage maximums occur at the same time and at that instant switching is avoided. This reduces switching power losses significantly. Figure 11 c) is so called continual clamping and it corresponds to reference pulse delay angle between 0-60˚ (In Figure 11 delay angle is 30˚). In continual clamping, clamped period occurs before sinusoidal modulating signal peak and it is most suitable for loads with power factor around 0.75. Again, to minimize switching power losses clamped time instant can be adjusted according to load power factor by adjusting the delay angle. Figure 11 e) is so called split-clamping where clamped time is divided to two equal time periods. Split-clamping is suitable for very inductive loads, where voltage and current maximum values occur 90˚ apart from each other. [20, 21]

If bus-clamping method is used and clamping technique is chosen efficiently according to the load nature, switching at maximum power points can be avoided. This reduces switching losses significantly. Because each phase leg is clamped at 1/3 of the fundamental period, the average switching frequency can be reduced to 2/3 of the theoretical carrier-signal frequency.

Generally, ratio of modulating signal frequency and fundamental frequency is defined

$$m_f = \frac{f_c}{f_1}, \tag{17}$$

where m_f is called frequency modulation ratio [2, p. 204]. If ratio m_f is an integer, modulation is called synchronous modulation. Usually, odd integers are preferred in synchronous modulation to avoid even harmonics. According to [2, p. 208], frequency modulation ratio is considered to be small if $m_f \leq 21$. In small frequency modulation ratio values, synchronous modulation should be used to avoid subharmonics i.e. harmonic frequencies below the fundamental frequency. This causes that for given fundamental frequency, modulation frequency cannot be exactly equal to reference modulation frequency if synchronous modulation condition is wanted to be satisfied. For higher values of m_f, amplitudes of subharmonics are considered to be negligible and m_f can be non-integer i.e. modulation can be asynchronous.

3.4.2 Inverter output voltage harmonics

Despite the clamped time instant, bus-clamping modulation doesn't produce significant additional switching harmonics to the output line-to-line voltages. Average switching frequency is generally 2/3 of the carrier frequency, but because switching pattern is implemented in a way that 2/3 of the fundamental period switching occurs at carrier frequency and 1/3 of the period phase is clamped and switching is avoided, voltage harmonics will not occur at average switching frequency and its multiples. Instead, output line-to-line voltage consists harmonics at multiples of fundamental frequency and around the carrier frequency and its multiples. Carrier-frequency harmonics and its multiples themselves are cancelled out in a three-phase system, because they are equal at every phase.

Output line-to-line voltage contains harmonics at multiples of fundamental frequency. Those harmonics are called base-band harmonics. Base-band harmonic frequencies can be defined in three-phase system according to

$$f_{BB} = vf_1 \text{ where } v = 2k + 1, v \bmod(3) \neq 0, k \in \mathbb{N}. \tag{18}$$

Definition (18) means that line-to-line base-band harmonics occur at non-triplen odd multiples of fundamental frequency [2, pp. 225–230]. Triplen harmonics are cancelled out because sum of them is zero in balanced three-phase system.

In addition to base-band harmonics, line voltage contains so called side-band harmonics at frequencies

$$f_{SB} = mf_c \pm nf_1 \text{ where } m \pm n = 2k + 1, n \bmod(3) \neq 0 \quad m,n \in \mathbb{Z}^+, k \in \mathbb{Z} \qquad (19)$$

Definition (19) means, that side-bands occur around carrier frequency and its multiples [19, p. 220]. Triplen side-band harmonics are cancelled out, because they are equal for every phase. Sum of n and m must be odd, so side-band harmonics are different in different bands.

In practice, definition (19) means that most significant side-band groups are

$$\begin{gathered} f_{SB1} = \{f_c \pm 2f_1, f_c \pm 4f_1\} \\ f_{SB2} = \{2f_c \pm f_1, 2f_c \pm 5f_1, 2f_c \pm 7f_1\} \\ f_{SB3} = \{3f_c \pm 2f_1, 3f_c \pm 4f_1\} \end{gathered} \qquad (20)$$

In (20) side-band orders of $n > 7$ are considered to be insignificant, because amplitudes of those harmonics are very small compared to lower frequency harmonics.

Based on the analysis above, side-band harmonics for the most common carrier frequencies for fundamental frequency of 160 Hz are shown in Table 2. Frequencies are calculated in cases where modulation frequency is equal to reference modulation frequency (asynchronous modulation) and where actual modulation frequency is chosen according to closest odd integer m_f (synchronous modulation). For 3000 Hz closest odd integer $m_f = 19$ and for 3500 Hz $m_f = 21$. For 4000 Hz, m_f becomes exactly 25, so synchronous modulation condition is naturally satisfied.

Table 2. *Significant side-band harmonics at different modulation frequencies for fundamental frequency 160 Hz.*

$f_{mod,ref}$(Hz)	3000		3500		4000
$f_{mod,actual}$(Hz)	3000	3040	3500	3360	4000
$f_{sw,ave}$(Hz)	2000	2027	2333	2240	2667
f_{SB1}(Hz)	2360	2400	2860	2720	3360
	2680	2720	3180	3040	3680
	3320	3360	3820	3680	4320
	3640	3680	4140	4000	4640
f_{SB2}(Hz)	4880	4960	5880	5600	6880
	5200	5280	6200	5920	7200
	5840	5920	6840	6560	7840
	6160	6240	7160	6880	8160
	6800	6880	7800	7520	8800
	7120	7200	8120	7840	9120
f_{SB3}(Hz)	8360	8480	9860	9440	11360
	8680	8800	10180	9760	11680
	9320	9440	10820	10400	12320
	9640	9760	11140	10720	12640

Amplitudes of side-band harmonics depend on system operating point, load current characteristics and possible overlapping of base-band and side-band harmonics. Usually base-band harmonic amplitudes decrease as the harmonic order increases. If the side-bands are far enough from the base-band harmonics, side-band harmonics closest to the side-band center can be considered to have largest amplitudes. However, this is not evident and the harmonic band overlapping might increase certain harmonic amplitudes significantly.

To investigate harmonic content of the inverter output voltage, line-to-line voltage was measured from the inverter output before the output sinusoidal filter at different fundamental frequencies. Normalized spectrum of output line-to-line voltage at 160 Hz is shown in Figure 12 and at 120 Hz in Figure 13.

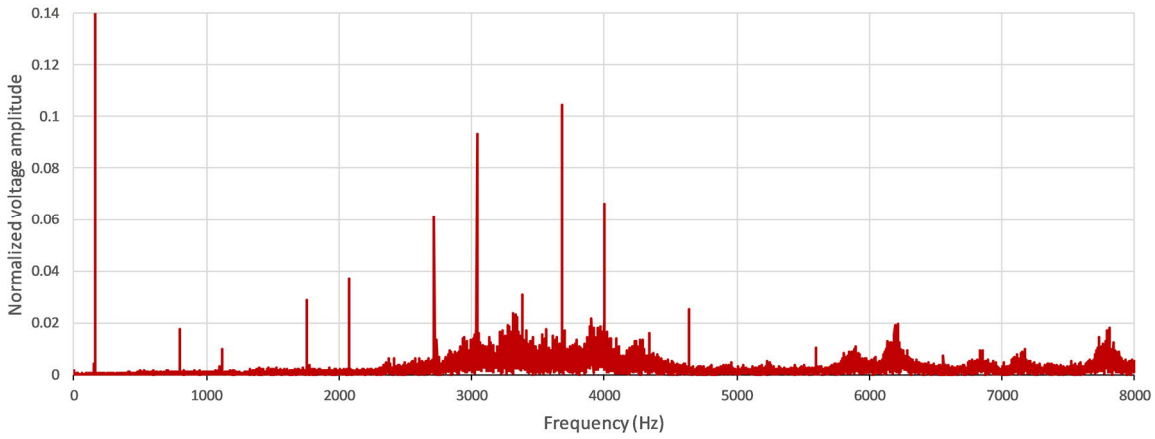

Figure 12. *Normalized spectrum of output line-to-line voltage before filter at 160 Hz.*

As seen from Figure 12, most significant harmonics occur at non-triplen multiples of fundamental frequency at frequencies between 3–4 kHz. Switching side-bands are visible in figure and side-band harmonics listed in Table 2 can be clearly seen. Amplitudes of those frequencies are insignificant compared to other harmonics. Harmonic pattern differs from theoretical analysis in (18)–(20) and there are two different main reasons for it.

With fundamental frequency of 160 Hz, frequency ratio m_f is small and some of the base-band harmonics occur inside first side-band group. Harmonics from two different sources are located at same frequencies and summed up causing harmonics with significant amplitudes. For example, 23rd fundamental harmonic frequency is inside 1st side-band. As a result, frequency 3680 Hz has relative amplitude of 10.5 % which is much higher compared to lowest base-band harmonics (amplitude of 5th harmonic is only 1.7 %). On the contrary, base-band harmonics don't affect harmonics in 2nd side-band and therefore those harmonic amplitudes seem to be insignificant. Maximum relative amplitude in 2nd side band is only 2 %.

Other reason for the harmonic pattern in Figure 12 is overmodulation. As described on Chapter 3.3, linear modulation range is exceeded at 160 Hz operation and some additional harmonics occur at side bands around the carrier frequency multiples. This makes side-band generally flatter but also wider. This causes even more base-band harmonics to occur inside the 1st side-band, which again increases harmonic amplitudes in 1st side-band. [2, p. 228]

Harmonic spectrum of the line voltage at 120 Hz in Figure 13 is very different compared to Figure 12. Carrier frequency doesn't seem to be exactly at reference value but somewhat lower, which implies that the carrier frequency is adjusted according to odd integer-principle. At 120 Hz significant base-band harmonics don't occur at first side-band because distance between modulation frequency and fundamental frequency is larger compared to 160 Hz operation. In addition, modulation is operated in linear region and additional harmonics due to overmodulation don't exist. For these reasons, relative amplitudes of highest harmonics are lower than at 160 Hz. Highest relative amplitude at 120 Hz is only 7.4 %. On the other hand, second side-band seem to be much more relevant compared to the 160 Hz operation. Side-band itself is denser i.e. harmonics seem to occur throughout the side-band. Highest relative amplitude in 2nd side-band is approx. 4 %, which is more than half of the highest amplitude in 1st side band.

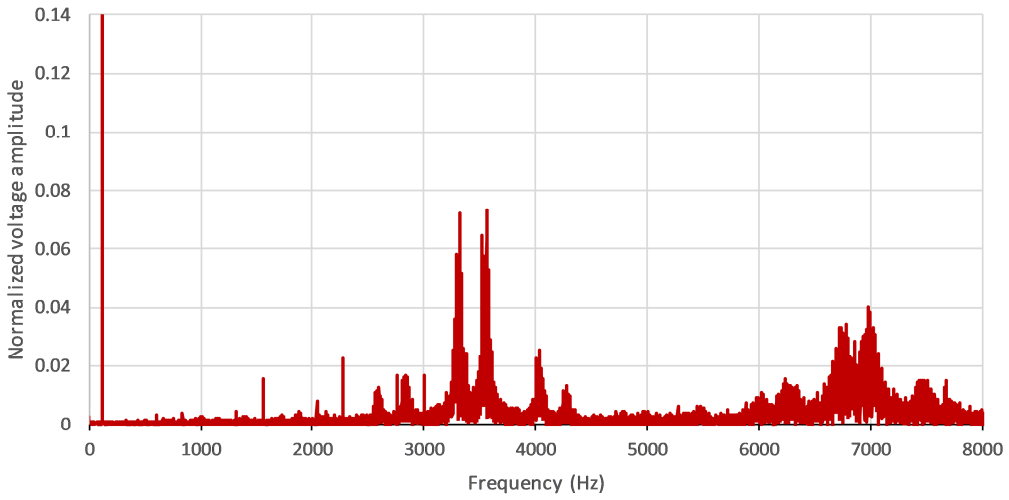

Figure 13. *Normalized spectrum of output line-to-line voltage before filter at 120 Hz.*

Relative amplitudes of most significant voltage harmonics with corresponding frequencies and relative amplitudes at both 120 Hz and 160 Hz are collected in Table 3.

Table 3. *Most significant harmonics of inverter output line-to-line voltages.*

160 Hz			120 Hz		
THD up to 50 kHz		47.35 %	THD up to 50 kHz		72.56 %
f (Hz)	Harmonic ord.	Relat. amplitude	f (Hz)	Harmonic ord.	Relat. amplitude
3680	23rd	10.5 %	3561	1st side band	7.4 %
3040	19th	9.3 %	3321	1st side band	7.2 %
4000	25th	6.6 %	7001	2nd side band	3.8 %
2720	17th	6.1 %	6782	2nd side band	3.4 %
2080	13th	3.7 %	4041	1st side band	2.6 %
3380	1st side band	3.1 %	2280	19th	2.3 %
1760	11th	2.9 %	3000	25th	1.7 %

As seen from Table 3, at high operating frequency fundamental harmonics are dominant due to overlapping with 1st side-band. In high-power high-speed applications where frequency modulation index is relatively low, harmonic frequency bands are quite wide. For example, according to Table 2, width of considered 1st and 3rd side-band groups are 1280 Hz and width of 2nd side-band group is 2240 Hz. Large frequency modulation ratio causes some fundamental frequency harmonics to be located frequency range of 1st side band and to be amplified significantly. Unlike applications where modulation frequency is high and fundamental frequency low, highest harmonics are not fundamental harmonics closest to fundamental frequency.

Unlike in Chapter 3.2, THD calculation up to 40th harmonic for VFD output voltage is not relevant, because waveforms are highly distorted. All significant harmonics don't occur at multiples of the fundamental frequency and calculation based on fundamental harmonics doesn't give accurate image about voltage distortion. Thus, THD is calculated

over whole frequency range up to 50 kHz. THD values at 160 Hz and 120 Hz are 47.35 % and 72.56 %. THD values are not complete comparable with THD values calculated up 40^{th} harmonic, but they give a good image about the amount of distortion. Fundamental frequency component can barely be seen from the waveforms.

Amplitudes of side-band harmonics depend on filtering, load characteristics and system operating point. According to [21], amplitude of most significant side-band harmonics varies within the operating frequency in bus-clamping modulation. At low fundamental frequencies, 1^{st} side-band harmonics are much more significant compared to 2^{nd} side-band. As the operation frequency increases, amplitude difference between side-band groups becomes smaller, which was also seen in measurement results in Table 3.

Overlapping effect of base-band and side-bands could be reduced or avoided by increasing inverter modulating frequency. As a result, voltage waveform would be more sinusoidal and base-band harmonic would not occur inside 1^{st} side-band. However, higher modulating frequency increases switching frequency and losses and depending on used VFD, increasing modulating frequency is not necessary even possible. FAT-setup VFD was shortly tested at modulating frequency reference of 4000 Hz. Based on voltage waveform, increasing modulating frequency from 3.5 kHz to 4 kHz doesn't improve output voltage waveform significantly and average switching frequency is increased more than 330 Hz. To achieve beneficial improvement of voltage waveform, modulation frequency should be increased even more, which is not even possible for used high-power VFD.

4. OUTPUT SINUSOIDAL FILTER

4.1 Filter structure and motivation to use filter

The inverter output filter is called sinusoidal filter (sine-filter) if its main purpose is to smoothen voltage and current waveforms close to sinusoidal. Same kind of filter structures are also called dv/dt-filters in some applications. Main purpose of dv/dt-filters is to limit fast voltage rises and falls i.e. limit the absolute value of dv/dt to be small. Sine-filters differ from dv/dt-filters in component size rather than in structure. [14, pp. 124–133]

In practice there are multiple different sine-filter structures, but the simplest sine-filter is a passive LC-filter. Capacitors can be connected in star or in delta configuration depending on the voltage level. In star, other terminal of each capacitor is connected to one of the phases and other terminals are connected together. In an ideal circuit, voltage over each capacitor is equal to the phase voltage. In delta connection, capacitors are connected between phases and voltage over capacitor is equal to the line voltage. Sine-filters with different capacitor configurations are shown in Figure 14.

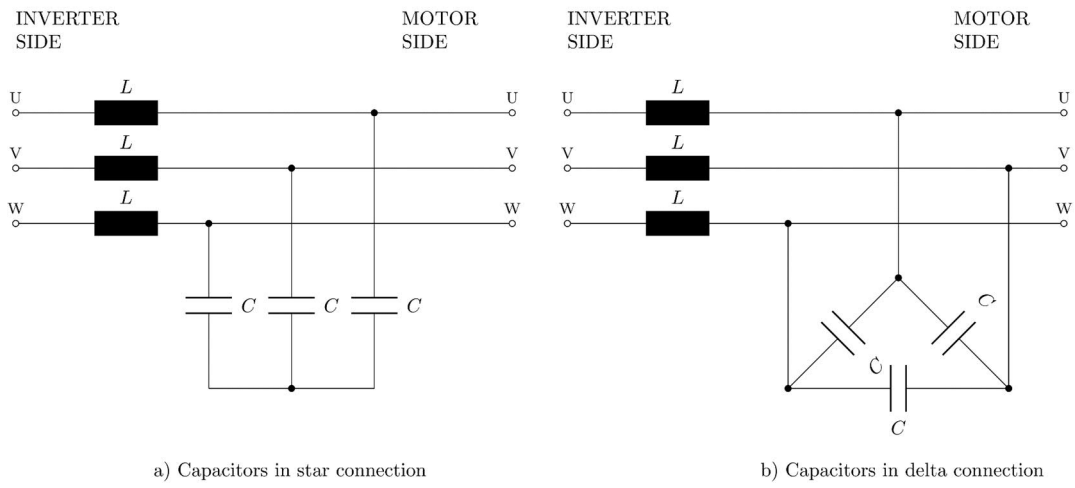

Figure 14. *Generic LC-sinusoidal filters with different capacitor configurations.*

Filter structures in Figure 14 behave as low-pass filters that provide a low-impedance path for high frequency components [22]. In Runtech's FAT-setup, sine-filter consist of multi-layer foil-conductor inductors and delta-connected capacitors. Each capacitor consists of multiple smaller capacitor modules connected in series.

Besides the smoothing of waveforms and limiting voltage transients, one major purpose of the sine-filter is to compensate motor magnetizing current i.e. correct power factor seen by the VFD. As mentioned in Chapter 2.2, especially the solid-rotor motor has poor power

factor. If power factor can be improved by filter design, the overall current of the system reduces. This directly affects current ratings of the inverter and other components in the system, which again might remarkably decrease total costs of the system. Highly distorted supply voltage can cause multiple undesired phenomena in motor applications. Major drawbacks are higher losses, decreased overall efficiency, bearing currents and other parasitic currents. Especially in solid-rotor motors high harmonic content of the supply voltage might cause major reduction of the motor performance. [22]

Generally, the solid-rotor motors have a small number of stator winding turns. For example, in EP-turbo solid-rotor motor there is only one turn per stator coil. Due to the low number of turns, stator inductance seen by the supply is small [1, p. 82]. Because stator inductance is small, distorted supply voltage leads to stator current of high harmonic content, which again creates distorted air-gap flux. Distorted air-gap flux including fast transients could create eddy currents to the rotor surface. As mentioned in Chapter 2.2, solid rotor core is made of a single solid piece of a ferromagnetic material. Due to this, rotor surface resistance is remarkably lower compared to conventional laminated rotor and solid rotor offers free paths to induced eddy currents.

According to [1, p. 62], harmonic eddy current losses are only couple per cents of the additional losses of the standard induction machine with laminated-steel motor. In solid-rotor motor however, harmonic eddy current losses might constitute even more than 10 % of the additional losses. Because of this, reduction of the eddy currents is critical in solid-rotor machine applications. Improving quality of the supply voltage and modifying voltage waveforms to be more sinusoidal are important factors while reducing eddy current losses. Output filtering plays an important role in this reduction.

One major cause of AC-motor failures is bearing failures and main reason for those are bearing currents. Bearing currents and other common-mode currents are currents that flow in electric circuit formed by inactive parts of the power system, parasitic capacitances and inductances and in most cases, ground or other ambient structures. The origin of common-mode currents are common-mode voltages, i.e. voltages which do not sum up to be zero and are in same phase in all three phases. Three-phase inverter output voltage produces common-mode voltages by nature because switching in different phases doesn't occur simultaneously. Output filter smoothens voltage pulses and limits voltage rate of change which reduces bearing currents effectively. [18, pp. 492–494] Ceramic bearing of EP-turbos mitigates bearing currents very well, but the motor supply system contains other paths for parasitic currents.

4.2 Filter effects on output voltage

Inverters produce naturally output voltage waveforms far from sinusoidal. Voltage changes rapidly as the inverter switching state changes. The switching pattern can be seen

from output voltage waveform especially with low inverter switching frequencies. The general reason for output filtering is to modify output voltage to become sinusoidal.

Figure 15 shows an example of three-phase output line-to-line voltage measured before and after output sinusoidal filter when fundamental frequency is 160 Hz and reference modulating frequency is 3500 Hz.

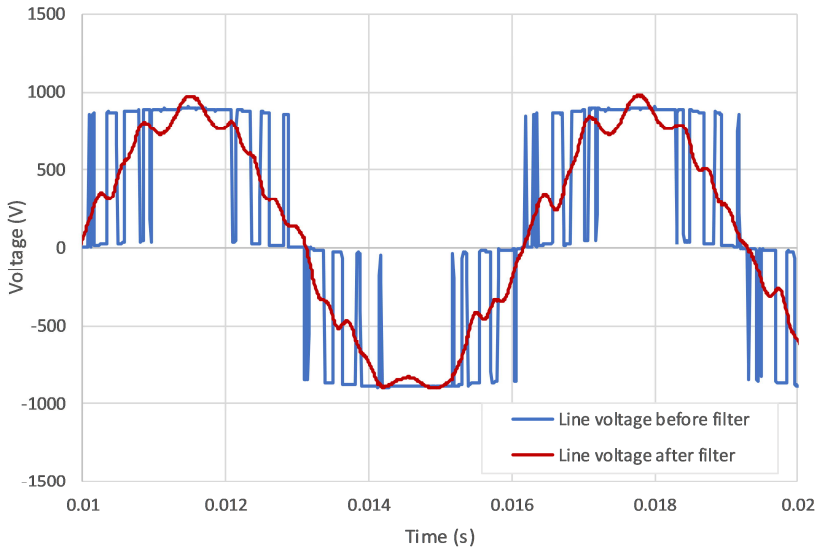

Figure 15. *Line-to-line voltage waveforms before and after sinusoidal filter.*

As seen from Figure 15, voltage waveform before filter is far from sinusoidal and fundamental frequency cannot be seen easily. Voltage after filter is still distorted but switching pulse pattern has disappeared and voltage is quite sinusoidal.

To investigate further how the filter affects the output voltage, voltage spectra of filter output line voltages were calculated. Normalized line voltage spectra after output sinusoidal filter at 160 Hz and 120 Hz are shown in Figure 16 and Figure 17.

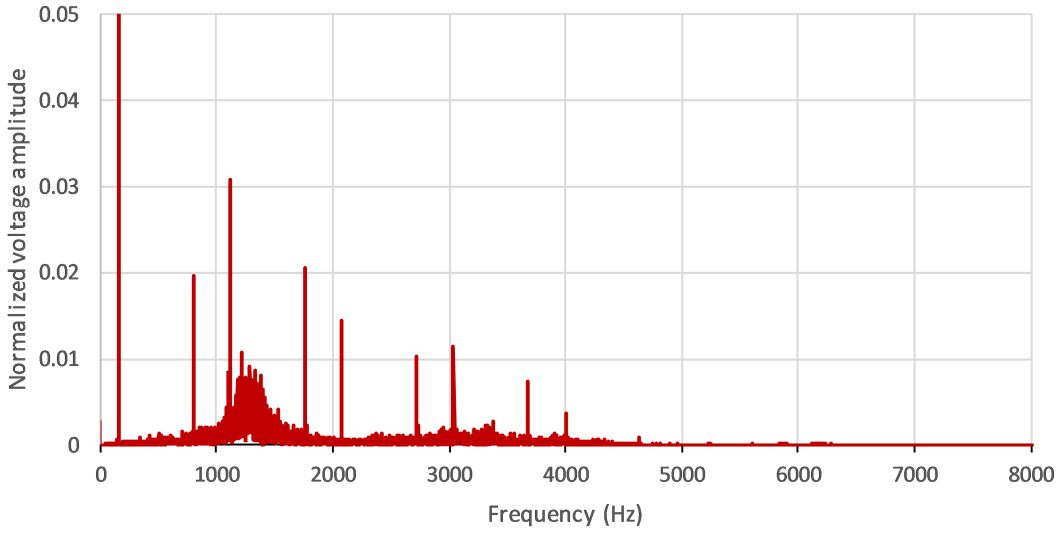

Figure 16. *Normalized line voltage spectrum after output filter at 160 Hz.*

If voltage spectrum after filter is compared to spectrum before filter (Figure 12), effect of the filter can be seen clearly. 1st side-band harmonics are very small and 2nd side-band has basically been filtered out. Base-band harmonics are the most dominant harmonics and filter barely affects the lowest base-band harmonic amplitudes.

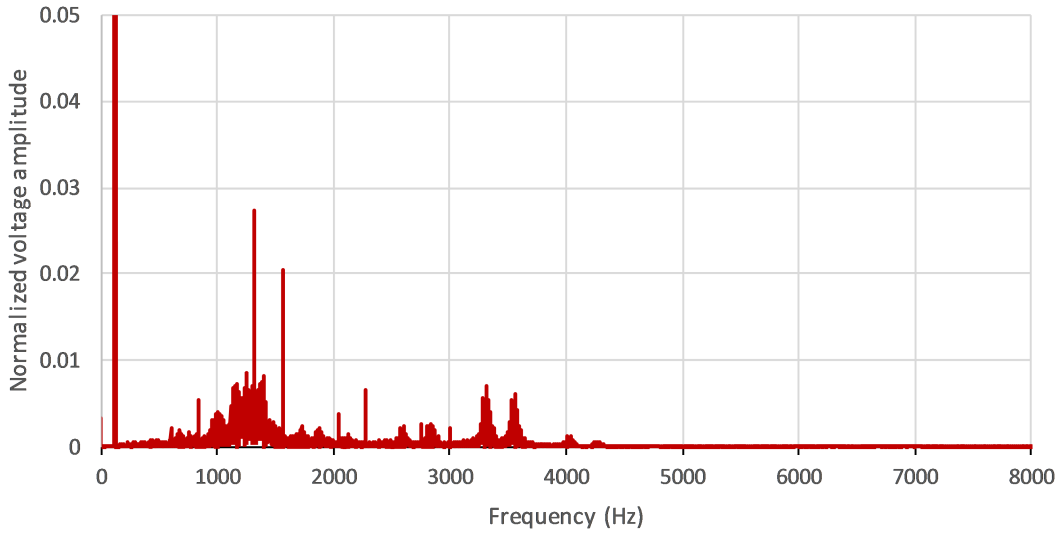

Figure 17. *Normalized line voltage spectrum after output filter at 120 Hz.*

In Figure 17, 1st side band is seen more clearly compared to Figure 16 but base-band harmonics are dominant also at 120 Hz. This is consistent with analysis in Chapter 3.4.2 where side-band harmonics were more visible at lower operating frequencies at analysis before filter. Compared to spectrum before filter (Figure 13), side-band harmonics are filtered very effectively, and base-band harmonics are somewhat equal before and after filter.

Analogously to Table 3, most significant harmonics of line voltages after filter at 160 Hz and 120 Hz are collected in Table 4. To be comparable with measurements before filter, THD values are again calculated over whole frequency range up to 50 kHz.

Table 4. *Most significant harmonics of filter output line-to-line voltages.*

160 Hz			120 Hz		
THD up to 50 kHz		9.76 %	THD up to 50 kHz		9.35 %
f (Hz)	Harmonic ord.	Relat. amplitude	f (Hz)	Harmonic ord.	Relat. amplitude
1120	7^{th}	3.1 %	1320	11^{th}	2.7 %
1760	11^{th}	2.1 %	1560	13^{th}	2.1 %
800	5^{th}	2.0 %	1249	base-band	0.8 %
2080	13^{th}	1.4 %	1397	base-band	0.8 %
3040	19^{th}	1.2 %	1164	base-band	0.7 %
2720	17^{th}	1.0 %	2280	19^{th}	0.7 %
3680	23^{rd}	0.7 %	3318	1^{st} side-band	0.6 %

When Table 3 and Table 4 are compared, it can be clearly seen how filter affects output voltage harmonic content. After filter amplitudes of most significant harmonics are much smaller and more importantly, harmonics above 2000 Hz are attenuated drastically. Filter used in measurement is originally designed to operate at 160 Hz, which explains why base-band harmonics are mitigated more at 160 Hz compared to 120 Hz operation. On the other hand, THD values at both operating points are somewhat equal and most importantly, THD values are decreased significantly. At 120 Hz, THD is decreased over 60 percentage points due to filtering.

4.3 Filter design

The main attribute that characterizes the filter performance is a resonant frequency. The resonant frequency is frequency, where inductive and capacitive reactances are equal and total impedance of the circuit is at its minimum. In LC-filter of Figure 14, the resonant frequency can be formulated as

$$f_{res} = \frac{1}{2\pi\sqrt{LC}}, \tag{21}$$

where f_{res} is resonant frequency of the filter, L is inductance of the filter inductor and C is the capacitance [14, p. 140]. Definition (21) can be directly used to calculate resonant frequency for star-connected capacitors. If capacitors are in delta, capacitance values must be first transformed to equivalent star-values.

In literature, there are multiple guidelines to choose filter resonant frequency. Generally, inverter output should not contain much energy at resonant frequency, because resonant frequency component could be amplified significantly. Filter resonant frequency should

be significantly higher than the fundamental frequency to avoid significant base-band harmonics to be in resonant frequency. On the other hand, resonant frequency must be lower than inverter modulating frequency to avoid side-band frequency components to occur in resonant frequency. According to [14, p. 140–141], guideline to choose resonant frequency is

$$\frac{1}{2} f_{sw} > f_{res} > 10 f_1. \tag{22}$$

Slightly differently formulated version (22) is presented in [22], where sufficient factor between resonant frequency and fundamental frequency is 5 instead of 10.

When filter parameter values are defined, there are multiple possible constraints to start with. If minimum current ripple is the most critical aspect, large enough inductance should be defined first [14, pp. 140–141]. Then again, if magnetizing current compensation is the key criterion, sufficient capacitor should be chosen first. According to [1, p. 86], for the solid-rotor motor a good rule of thumb is to choose capacitance to compensate 80 % of the current without load and inductance to be half of the stator's leakage inductance. This should lead to proper filter resonant frequency for a solid rotor motor.

There is, and always will be, a major trade-off between sine-filter performance and additional losses. According to (21), same resonant frequency can be achieved with infinite amount of LC-pairs. Generally, larger inductance value enables smoother current waveform and larger capacitor can compensate more magnetizing current. On the contrary, the larger the inductance value is, the larger is the voltage drop over filter. This voltage drop reduces the effective voltage in motor terminals, which again might reduce motor output power and torque. For this reason, the inductor value should be chosen to be as small as possible in terms of filtering constraints. Too large capacitor value might lead to over-compensation in low-speed or low-power situations and that might cause multiple problems such as increasing the common-mode currents. Very often larger component values increase filter losses and component costs.

4.4 Filter losses

Filter power losses can be naturally divided into inductor losses and capacitor losses. Inductor losses can be again divided into winding losses caused by resistive losses in inductor windings and core losses which occur in filter inductor core. Furthermore, core losses can be divided into eddy current losses, hysteresis losses and so-called excess losses.

Filter loss considerations are especially important in terms of temperature and cooling conditions. Filters are often placed into a narrow chassis where natural convection is not very effective. If cooling system is not dimensioned according to filter power losses, filter

temperature might become too high. On the other hand, filter power losses reduce effective power that could be fed to the load or in other words, additional power must be drawn from supply to cover filter power losses.

4.4.1 Inductor winding losses

Base of the winding losses are ohmic losses caused by conductor resistance. For arbitrary conductor, DC-resistance can be calculated by

$$R_{DC} = \frac{\rho l_c}{\pi A_c}, \tag{23}$$

where ρ is the resistivity of the conductor material, l_c is length of the conductor and A_c is conductor cross-sectional area [23, p. 421]. DC-resistance of the conductor can also be measured with multimeter.

In AC-applications, effective cross-sectional area of the conductor is smaller than actual conductor area due to the skin and proximity effects. Alternating current tends to flow near the conductor surface and current density is higher closer the surface than in the middle. Skin depth, i.e. depth from conductor surface where $\frac{1}{e}$ -part of the whole current flows, can be calculated by

$$\delta = \sqrt{\frac{\rho}{\pi f \mu}}, \tag{24}$$

where f is the frequency of the current and μ is the absolute permeability of the conductor material [1, p. 95]. In addition to skin effect, the proximity effect caused by adjacent conductors of the inductor decreases effective cross-sectional area of the conductor. Proximity effect is a result of varying magnetic field caused by adjacent current carrying conductors and it depends on inductor geometry, distance of bare conductors, skin depth and number of conductor layers of the inductor [2, p. 771].

Procedure to calculate AC-effects of the overall resistance is presented in [24, p. 39]. For the multi-layer foil-conductor inductor, the ratio of AC-resistance and DC-resistance can be approximated

$$\frac{R_{AC}}{R_{DC}} = \Delta\left(\frac{\sinh(2\Delta) + \sin(2\Delta)}{\cosh(2\Delta) - \cos(2\Delta)} + \frac{2}{3}(n^2 - 1)\frac{\sinh(\Delta) - \sin(\Delta)}{\cosh(\Delta) + \cos(\Delta)}\right), \tag{25}$$

where n is number of foil layers and Δ is ratio of foil thickness and skin depth, $\Delta = \frac{d_f}{\delta}$ where d_f is foil thickness.

If filter inductors are wounded with round conductors instead of thin foil, (25) can be used if factor Δ is replaced with $\Delta_r = \left(\frac{\pi}{4}\right)^{\frac{3}{4}} \frac{d_r}{\delta} \sqrt{\frac{d_r}{l_r}}$, where d_r is diameter of round conductor and l_r is distance between adjacent conductors. Number of foil layers n is replaced with number of conductor layers. [24, p. 25]

After the resistance-ratio calculation, winding losses of three-phase inductor caused by sinusoidal current can be calculated by [2, p. 34]

$$P_{winding} = 3R_{AC}I^2. \tag{26}$$

According to (24), skin depth depends on the current frequency and (25) implies that the AC-resistance also depends on frequency of the current. If current is non-sinusoidal, power losses of different current frequency component should be computed separately. For output inductor of PWM-inverter, losses of the fundamental frequency current and harmonic current components should be calculated separately and added together.

4.4.2 Inductor core losses

Evaluation of inductor core losses is far from straightforward. Core losses depend on magnetic flux density, supply current frequency and its harmonic content, material properties and physical structure of the core. Despite multiple factors affecting core losses, there are ways to approximate core losses analytically if supply current content is known accurately enough.

Magnetic field and magnetic flux density are linked together in constitutive equation

$$B = \mu_r \mu_0 H \tag{27}$$

where B is magnetic flux density, H is magnetic field and μ_r and μ_0 are relative permeability of the material and permeability of free space, $\mu_0 = 4\pi \cdot 10^{-7} \frac{\mathrm{H}}{\mathrm{m}}$ [2, p. 47].

To calculate maximum flux density at each frequency in three-phase filter core, core must be modelled as a reluctance network including reluctances of different parts of the core and air-gaps. Generally, reluctance of the magnetic component can be calculated as

$$\Re = \frac{l_{core}}{\mu_r \mu_0 A_{core}}, \tag{28}$$

where l_{core} and A_{core} are length and cross-sectional are of the analyzed component [2, p. 49]. In the air-gap, flux lines might bend, and effective cross-sectional area of flux-path is larger than in actual area of core material. This effect decreases air-gap reluctance and is called fringing flux. Fringing flux effect in rectangular core can be approximately taken

into account by calculating area in (28) using core dimensions and adding air-gap length to core width and depth. [2, p. 764]

Current flowing through the inductor can be modelled as a source of magnetomotive force

$$F_m = Ni = \Re\Phi \tag{29}$$

where Φ is magnetic flux [2, p. 49]. (29) defines the relation between magnetomotive force and magnetic flux and it is analogous to Ohm's law in electric circuits. Analogously with the Kirchoff's voltage and current laws, sum of magnetomotive forces around closed-loop in magnetic circuit equals zero and sum of incoming and outgoing magnetic fluxes at each point in magnetic circuit equals zero [2, p. 50]. Thus, the same analysis with electric circuits can be used to solve quantities in three-phase filter core.

Simplified reluctance network and magnetic circuit of generic three-phase filter core is shown in Figure 18. Due to confidentiality, detailed structure of actual core and core dimensions were left out.

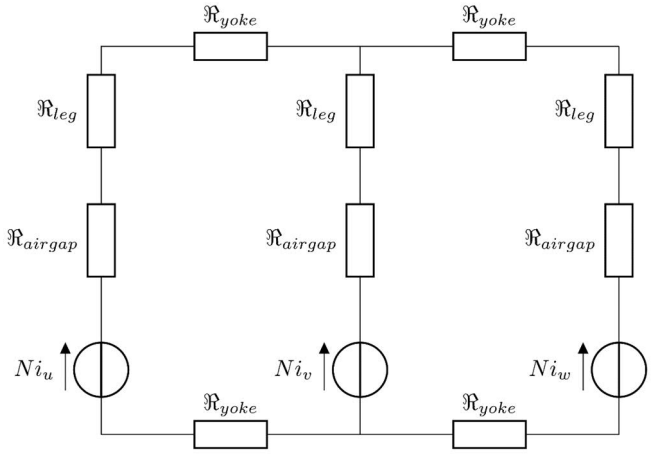

Figure 18. *Simplified magnetic circuit of generic three-phase core.*

In Figure 18, i_x denotes instantaneous inductor current at each phase. $\Re_{airgap}$ takes into account reluctance of air-gap or sum of multiple air-gaps in one core leg while $\Re_{leg}$ combines remaining core leg reluctance and reluctance of core corner. $\Re_{yoke}$ accounts reluctance of horizontal core bar between two core legs. Figure 18 assumes that reluctances of each legs and yokes are equal, which is relevant assumption if filter is designed for symmetric three-phase system.

Magnetic fluxes in the outermost filter core leg can be solved from magnetic circuit equations and flux in the center leg equals sum of two other fluxes if leakage fluxes are neglected. If all reluctances and currents are known according to Figure 18, fluxes at outermost core legs can be calculated in matrix form

$$\begin{bmatrix}\Phi_u\\ \Phi_w\end{bmatrix}=\begin{bmatrix}-(\Re_{ag}+\Re_{leg}+\Re_{yoke}) & \Re_{ag}+\Re_{leg}+\Re_{yoke}\\ -(2\Re_{ag}+2\Re_{leg}+\Re_{yoke}) & -(\Re_{leg}+\Re_{ag})\end{bmatrix}^{-1}\begin{bmatrix}N(i_w-i_u)\\ N(i_v-i_u)\end{bmatrix} \quad (30)$$

With assumptions of negligible leakage fluxes, flux density at each leg can be calculated

$$B=\frac{\Phi}{A_{core}} \quad (31)$$

Analysis above can be easily used in sinusoidal supply currents. Non-sinusoidal current can be divided to sinusoidal components at different frequency using DFT. Then, resulting magnetic flux densities at different frequencies can be calculated and total flux densities can be formed by summing up sinusoidal flux densities at different frequencies.

When flux density magnitude in certain frequency is known, total core losses per unit weight under sinusoidal excitation can be analytically approximated to be

$$E_{core}=\alpha B_{peak}^2 f+\frac{\pi^2\sigma_{core}d^2}{6\rho_{core}}B_{peak}^2 f^2+\beta B_{peak}^{1.5}f^{1.5} \quad (32)$$

where E_{core} is specific loss density of the core $\left(\frac{\mathrm{W}}{\mathrm{kg}}\right)$ and α and β are coefficient, σ and ρ_c are core conductivity and density and d is the lamination thickness of core [25, pp. 22–23]. In (32), first term represents hysteresis losses of the core and it is a modification of classical Steinmetz equation [2, p. 735, 26]. Second term presents eddy current losses in core and is proportional to square of the lamination thickness [2, p. 750]. Third term is called excess loss term and it includes loss sources which are not included in first and second term, such as losses generated by external field produced by moving magnetic domain walls. [25, p. 23]

Coefficients α and β in (32) are unknown, but they can be approximated if any data of specific losses in core material is available. When filter used in Runtech's FAT-setup is considered, filter core material manufacturer provides loss data curves as a function of magnetic polarization at frequencies 50 Hz and 60 Hz. Definition (27) can be re-arranged and modified by

$$J_m=B-\mu_0 H \quad (33)$$

where J_m is magnetic polarization [25, p. 19]. When external magnetic field is small, last term in (33) is really small and $J_m \approx B$. Then, provided specific loss curves can be used to estimate coefficients in (32). Coefficients were estimated using least-square-error -fitting. To minimize error caused by manual reading of the loss data, coefficients were calculated based on both 50 Hz and 60 Hz data and then averaged coefficients were used.

As a result, coefficients α and β were determined. Due to confidentiality, actual values of coefficients and core parameters in (32) were left out.

When coefficient values are found, total core losses at certain frequency can be calculated

$$P_{core} = E_{core} m_{core}, \tag{34}$$

where m_{core} is total mass of core. If core flux densities in different parts of core are significantly unequal, losses can be calculated by calculating losses at different flux density values and summing them up.

Because specific loss coefficients were estimated based on low-frequency loss data, possible errors get larger while frequency increases. Also due to the nature of (32), core losses at high frequencies are huge. Thus, even insignificant ripple or measurement noise could cause additional error to total core losses. At high frequencies loss calculation accuracy and measurement data quality should be considered carefully to avoid computational errors.

4.4.3 Capacitor losses

Capacitor active power losses can be modelled with equivalent series resistance (ESR) of the capacitor [2, p. 348]. ESR-value can be calculated

$$R_{ESR} = \tan(\delta_c) \frac{1}{2\pi f C}, \tag{35}$$

where δ_c is the load angle of the capacitor i.e. angle between capacitor total impedance and capacitive reactance. Load angle can be defined by measuring the phase shift between current and voltage.

Depending on the application, capacitor ESR might depend on operating frequency. Due to that, power losses caused by ESR can be calculated

$$P_{ESR} = \sum_{k=1}^{n} R_{ESR,k} I_k^2, \tag{36}$$

where P_{ESR} is sum of losses caused by different current components and I_k is RMS-value of k^{th} harmonic current component [27]. In high power applications capacitor ESRs are typically very small. Parallel capacitor bank current is also small compared to inductor current. Based on previously carried temperature measurements, output filter capacitors don't seem to warm up and for simplicity it can be assumed that capacitor power losses are negligible compared to inductor losses.

4.5 Filter loss calculations

To investigate filter power losses, filter currents and phase voltages from filter output were measured at different operating points between 60–160 Hz. Calculations were carried out using procedure described in Chapter 4.4. EP-turbo was supplied with nominal line voltage 690 V. Filter inductor current waveform at 160 Hz is shown in Figure 19 and normalized harmonic spectrum in Figure 20.

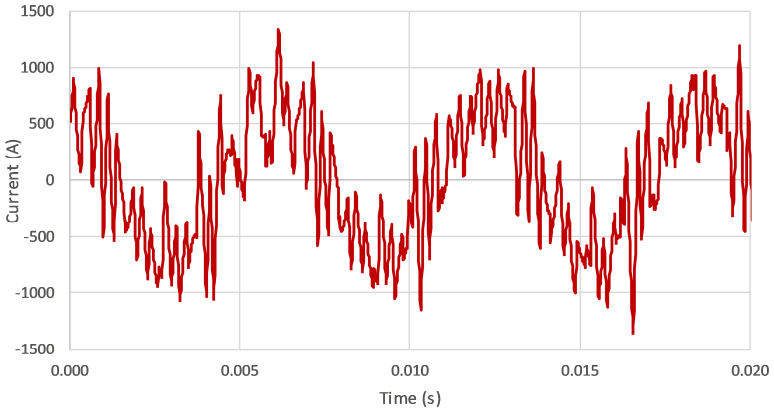

Figure 19. *Filter current at 160 Hz and 482 kW.*

As seen from Figure 19, filter current contains large ripple and some high spikes. Some significant harmonic frequencies are present in current waveform. Therefore, it is not relevant to approximate filter current only as a fundamental frequency component.

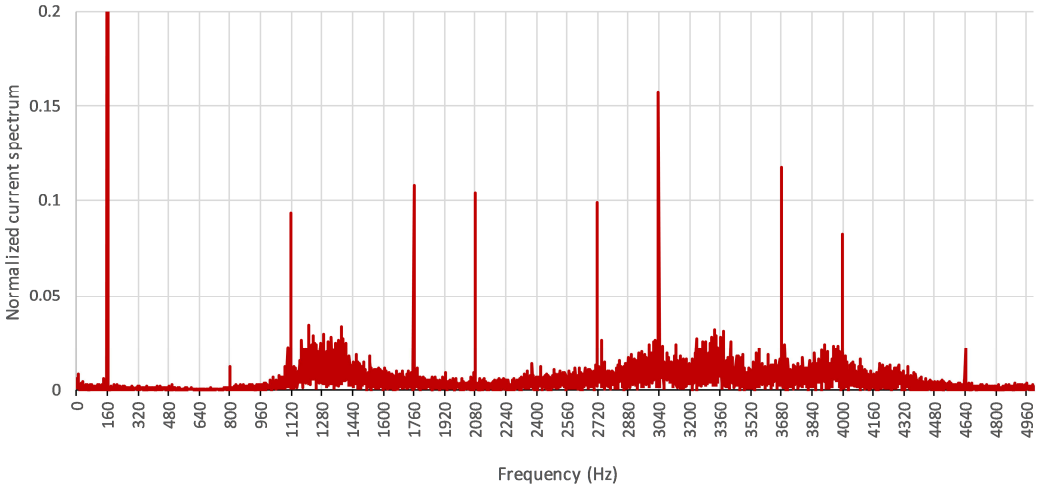

Figure 20. *Normalized current spectrum at 160 Hz and 482 kW.*

Current spectrum in Figure 20 shows that current contains significant 7^{th}, 11^{th} 19^{th} and 23^{rd} harmonics. At 160 Hz fundamental frequency 19^{th} (3040 Hz) and 23^{rd} (3680 Hz) harmonic amplitudes are especially high because they are located at the first switching frequency side-band. Compared to voltage spectrum in Figure 16, filter current contains

same base-band harmonics despite that relative amplitudes of current harmonics are slightly higher. In addition, current spectrum contains wide range of small amplitude harmonics between 1000–4000 Hz.

Due to the harmonic content, it is not reasonable to evaluate filter power losses based on only fundamental frequency current. Instead, current was split into sinusoidal harmonic components using amplitude invariant DFT. Then, (32) was applied to each current component separately. Filter power losses at each frequency were then summed up to evaluate total power losses.

Based on DFT, filter current contents at each operating point are shown in Table 5. Last column is RMS-value of measured phase voltage from filter inductor output respect to inverter ground.

Table 5. *Current and voltage data at different frequencies, 690 V supply.*

$f_{oper.}$ (Hz)	I_{RMS} (A)	I_{RMS1} (A)	I_{RMS1}/I_{RMS}	$U_{RMS,phase}$ (V)
60	444	320	72.14 %	150.1
80	469	338	72.05 %	197.2
100	507	364	71.75 %	245.8
120	496	398	80.22 %	292.7
140	535	430	80.33 %	344.1
160	548	471	85.96 %	367.8

As seen from Table 5, the higher the operating frequency and the supply voltage are, the larger is the ratio of fundamental current component and total current RMS. This means that at lower frequencies relative harmonic current is larger compared to the higher frequencies. This effect is generally due to filter compensation capacity. Filter parameters are fixed, and filter is dimensioned based on 160 Hz operation. At lower frequencies and voltages filter compensation doesn't affect very much and current contains more harmonic components.

Table 6 provides calculated power and power loss data at different operating points. To avoid computational errors due to measurement noise and other high frequency disturbances, filter core losses were calculated only up to 7.5 kHz. This simplification shouldn't reduce accuracy of the calculation, because if amplitudes of different current components are summed up, it can be seen that more than 98 % of the total energy is transferred at frequencies below 7.5 kHz.

Table 6. *Calculated power data at different frequencies, 690 V supply.*

$f_{oper.}$ (Hz)	$P_{filt.}$ (kW)	$P_{filt.1}$(kW)	$P_{filt.1}/P_{filt.}$	$\Delta P_{filt.}$(kW)	$\Delta P_{filt.1}$(kW)	$\Delta P_{filt.}/P_{filt.}$
60	52.3	49.7	95.06 %	6.96	0.27	13.30 %
80	103.1	100.4	97.42 %	7.77	0.30	7.54 %
100	174.4	171.1	98.12 %	8.39	0.36	4.81 %
120	263.8	262.1	99.35 %	7.43	0.43	2.82 %
140	370.2	366.8	99.08 %	6.34	0.51	1.71 %
160	481.5	479.0	99.48 %	5.94	0.62	1.23 %

As seen from Table 6, most of the power at each operating point is transferred at fundamental frequency. However, at higher frequencies relative fundamental frequency power is even higher and at nominal operating point more than 99 % of active power is supplied at the fundamental frequency. This is consistent with behavior of the relative fundamental current in Table 5. On the other hand, most of the active power losses (ΔP_{filt}) are caused by the harmonic current components and only relatively small portion of losses are caused by the fundamental current. Relative filter active power losses are shown in last column in Table 6. The closer the operating frequency is to nominal frequency, the smaller are relative power losses.

Detailed filter power loss data is shown in Figure 21. Based on current measurements and power loss calculations, maximum active power losses occur at operating frequencies around 100 Hz. At nominal frequency, total filter power losses are almost 2.5 kW smaller compared to maximum power losses at lower frequencies.

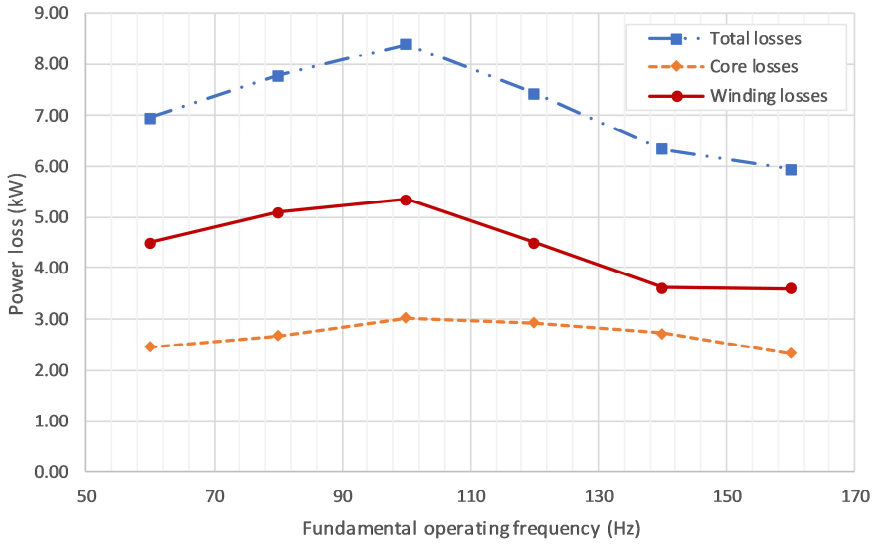

Figure 21. *Filter power losses at different frequencies, 690 V supply.*

Both core losses and winding losses increase up to 100 Hz and beyond that losses start to decrease again. Filter loss waveform can be explained by fixed filter components. Capac-

itors are dimensioned to operating points near the nominal frequency. At lower frequencies, filter capacitors cannot produce much compensation and filter current is higher at 100 Hz compared to 120 Hz. Because capacitor currents are smaller at lower frequencies, filter currents are relatively larger and more importantly, current harmonic contents are higher. In addition to the capacitors, inductors themselves are dimensioned to operate near nominal frequency and at lower frequencies filter reactance is smaller. This leads to higher harmonic content and less sinusoidal current waveforms. Because both effective AC-resistance and core losses are highly dependent on current frequency, filter active power losses are higher at 100 Hz compared to nominal 160 Hz, even though current RMS at 100 Hz is only 93 % of current RMS at 160 Hz.

Filter power losses caused only by fundamental frequency current component at each operating point are shown in Figure 22. Fundamental frequency power losses increase consistently among the operating frequency and filter power. As it can be seen from figure, most of the fundamental frequency power losses are winding losses. This is due to the fact that most of the core loss components in (32) proportional to the square of operating frequency and at low frequencies core losses remain very small.

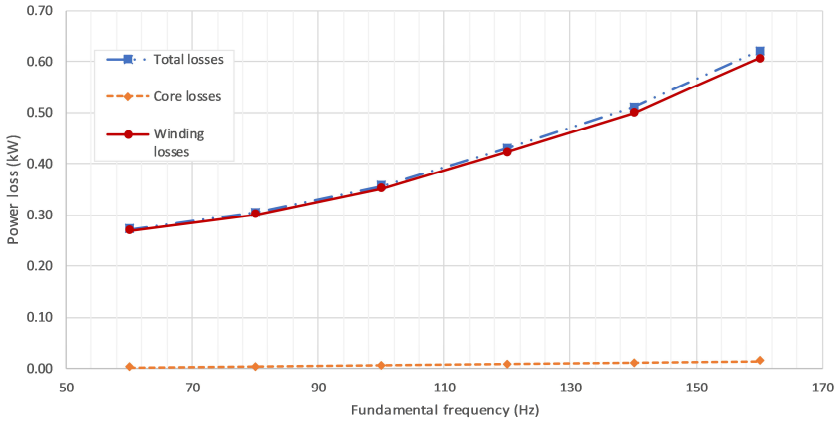

Figure 22. *Filter power losses due to fundamental current.*

Figure 23 provides a conclusion of power loss calculations at different frequencies. As it can be seen, power drawn from the filter increases among the operating frequency and so does the fundamental frequency current. At the same time, total current RMS increases slower and even decreases from 100 Hz to 120 Hz. This different sized gap between total current and fundamental current can be used to explain the nature of power losses at different operating points. In the middle of the frequency range, higher amount of energy is located at higher frequencies and due to frequency dependency of the losses, highest filter losses occur well below the nominal frequency.

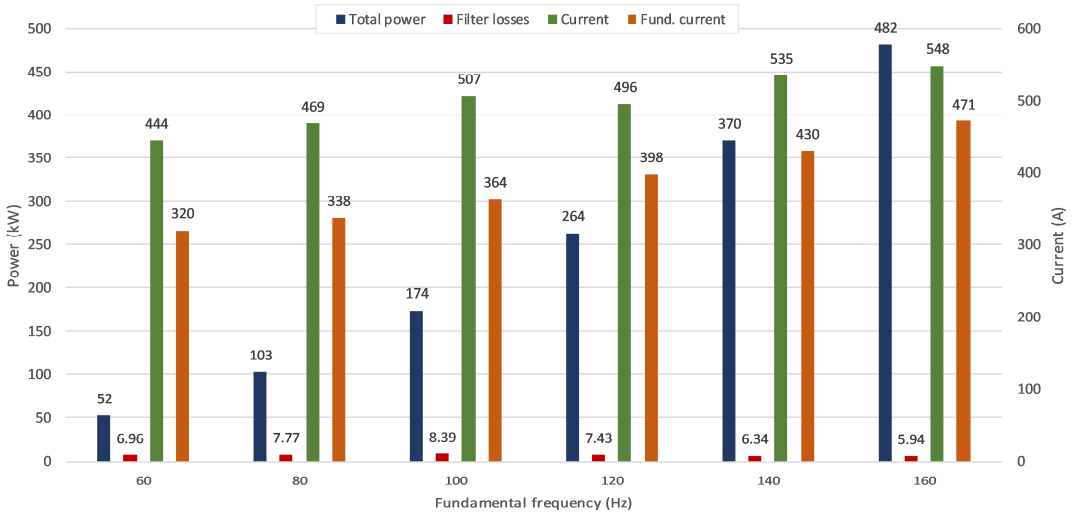

Figure 23. *Currents, powers and power losses at different frequencies.*

Even though the nominal supply frequency of the largest EP-turbos is 160 Hz, in some application they are supplied by 120 Hz voltage. Supply frequency can be even 100 Hz at some rare cases. Because filter power loss maximum is located near 100 Hz, efficiency of the filter is much lower at 100 Hz or 120 Hz operations compared to nominal operation. Higher losses must also be taken into account in cooling conditions. If turbos are constantly operated at lower frequencies, more cooling air flow might be required to avoid filter chassis overheating.

In addition to the filter loss comparison at different operating points, filter power losses were calculated while EP-turbo with nominal voltage of 400 V was tested. Table 7 provides calculated current and power data for both 690 V and 400 V measurement at 160 Hz. Calculated filter inductor power difference of two measurements at different turbos was 52.9 kW. Filter output power was higher in the 400 V measurement.

Table 7. *Current and power data at different supply voltages, 160 Hz.*

$V_{phase,RMS}$ (V)	I_{RMS}(A)	I_{RMS1}(A)	I_{RMS1}/I_{RMS}	ΔP_{filter}(kW)	P_{filter}(kW)	$\Delta P_{filt}/P_{filt}$
400	1141.7	1100.5	96.39 %	10.06	534.4	1.88 %
690	550.1	471.5	85.71 %	5.11	481.5	1.06 %

As seen from the Table 7, filter current is significantly higher when 400 V is used, which is obvious while total powers are somewhat equal. Relative harmonic current is lower at 400 V, but filter power losses are almost doubled compared to 690 V because current is more than twice as high as in 690 V. Just like Figure 23, Figure 24 provides a comparison of power losses and currents at 400 V and 690 V supplies. At 400 V, average line current is 208 % higher than current at 690 V while the filter power is 111 % higher respectively. Filter power losses at 400 V are 197 % higher in the same measurements.

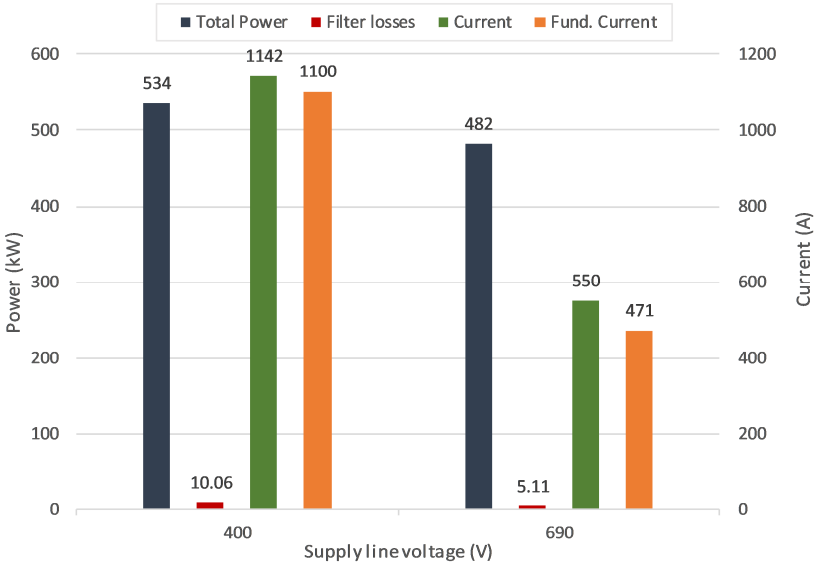

Figure 24. *Currents, powers and power losses at different voltages, 160 Hz.*

Filter loss nature from Figure 21 and loss data at different voltages from Figure 24 combined together imply that highest absolute filter power losses occur at 400 V supply and operating frequency around 100 Hz. For relevant operating points that are used constantly, filter losses are highest at 120 Hz and 400 V supply. Filters used in different application are somewhat different, but general behavior of the filter losses remains the same. For fixed sinusoidal filter, highest losses occur at frequencies below nominal due to filter dimensioning and compensation.

Power loss calculations in this chapter are based on multiple simplifications and analytical solutions. Therefore, absolute values of filter power losses might include some errors. Despite that, calculations show clearly the nature of filter power losses frequency dependency while operating point of EP-turbo is varied over relevant frequency and power ranges. In a future, calculations can be used to evaluate power losses in different filters or at least to calculate so-called worst-case scenario losses i.e. maximum power losses that could occur in certain application.

4.6 Filter voltage drop

Instantaneous voltage drop over filter inductance can be calculated

$$\Delta V_{f,L}(t) = R_{AC} i_{inv}(t) + L \frac{di_{inv}(t)}{dt}\,, \tag{37}$$

where $\Delta V_{f,L}(t)$ is instantaneous voltage drop over filter inductor, $R_{L,AC}$ is AC-resistance of inductor foil and $i_{inv}(t)$ is instantaneous inverter current [2, p. 53]. Because voltage before filter inductor is highly pulsating, voltage waveforms are very different before and after filter inductors as shown in Figure 15. For this reason, instantaneous voltage drop

or total difference of voltage RMS-values are not very relevant quantities. Instead, relevant voltage drop can be evaluated by considering voltage drop at fundamental frequency. This is also the frequency where most of the power is transferred as shown in Chapter 4.5.

RMS-value of the voltage drop can be modelled as a sum of voltage drops caused by different harmonic current components. Fundamental frequency voltage drop can be calculated

$$\Delta V_{f1} = Z_{f1} I_1 = \sqrt{R_{AC}^2 + (2\pi f_1 L)^2} I_1 \tag{38}$$

Because highly pulsating filter input voltage, evaluation of fundamental voltage drop based on voltage difference is difficult. Thus, it's more accurate to evaluate fundamental voltage drop based on (38) and fundamental current component. AC-resistance of inductor foil can be calculated in a way described in (25) but because only fundamental frequency voltage drop is considered, AC-resistance is only couple per cents higher than DC-resistance. Thus, voltage drop calculation results are basically equal if only DC-resistance is used.

Calculated absolute and relative fundamental frequency voltage drops at different operating points are shown in Table 8. Measured inductor output phase voltage and inductor current are also presented.

Table 8. *Filter fundamental voltage drop calculation.*

f_{oper} (Hz)	$V_{1,ph}$(V)	$I_{1,rms}$(A)	$\Delta V_{1,rms}$ (V)	$\Delta V_{1,rms}/V_{1,ph}$
60	146	320	3.4	2.3 %
80	194	338	4.8	2.5 %
100	242	364	6.4	2.6 %
120	291	398	8.4	2.9 %
140	342	430	10.6	3.1 %
160	366	471	13.3	3.6 %

As seen from Table 8, both absolute and relative fundamental voltage drops increase as operating frequency and phase voltages increase. This is because fundamental current increases among the supply frequency. To better illustrate voltage drops at different operating points, filter output phase voltage and filter voltage drop are shown in Figure 25 as a function of operating frequency.

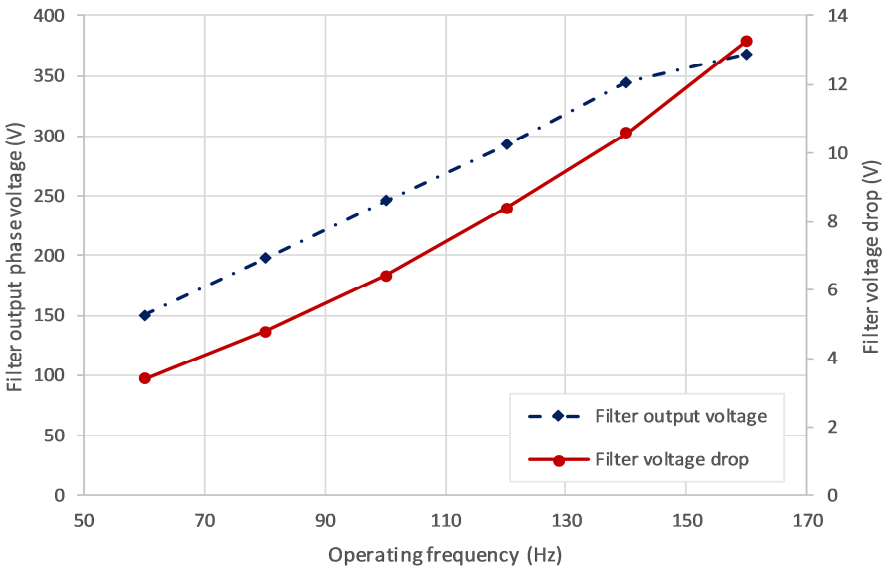

Figure 25. *Filter fundamental phase voltage and voltage drop.*

Figure 25 shows that filter output phase voltage increases linearly according to U/f-control scheme up to 140 Hz. After that, overmodulation region is achieved and voltage-curve increases with smaller angle. As seen from Table 8, filter current increases more at frequencies close to nominal frequency compared to lower frequencies. Due to this, fundamental voltage drop increases almost linearly at low frequencies and as frequency becomes close to nominal, fundamental voltage drop increases faster.

Generally, relative filter voltage drop is not very large and relative phase voltage drop varies between 2–4 % over operating frequency range. If whole supply chain from the transformer to the motor terminals is considered, filter voltage drop is only one source of voltage drop. On the other hand, at nominal operating frequency, overmodulation is required to achieve nominal supply voltage and at same operating point filter voltage drop is at its highest. Filter voltage drop lowers the point where linear modulation range must be exceeded.

4.7 Reactive power compensation

As described in Chapter 2.2, the power factor of any induction motor is less than one due to rotor magnetization. This means that induction motor is naturally seen as an inductive load by the supply system. Inductive power factor of the load means, that supply voltage leads load current as described in chapter 3.1. Power factor seen by the supply can be improved by compensating reactive current demand using output filter.

According to (10), reactive current increases total current. Higher total current increases ohmic losses and according to (26), ohmic conduction losses are proportional to square of the current RMS-value. Due to higher total current, supply cable loading capacity must be higher, which might require thicker and more expensive cables. Higher total current

can also demand higher power rating and current handling capability of the supply inverter. Thicker cables and inverter with higher power rating generally increase overall costs of the system.

Reactive power demand can be partly compensated with the sine filter capacitors. Due to their electromagnetic nature, capacitor current leads capacitor voltage by 90˚ and when capacitors are connected parallel with the supply line, leading current drawn by capacitors compensate at least some of the lagging current of the inductive load. As a result, total current drawn from the supply is decreased by magnitude and total power factor seen by supply system becomes closer to unity. [2, pp. 36–37]

In fixed-capacitor compensation same capacitors are connected in parallel with the load all the time, even if the load characteristics are changed. Absolute value of fundamental frequency reactive power produced by three-phase capacitor bank or sinusoidal filter can be calculated by

$$Q_c = \frac{3U_c^2}{X_c} = 6\pi f U_c^2 C \tag{39}$$

where U_c is voltage over capacitor and X_c is capacitive reactance [2, p. 37]. As seen from (39), produced reactive power is proportional to supply frequency and capacitor capacitance and proportional to capacitor voltage square. If capacitors are delta-connected, capacitor voltage is approx. line voltage and in star-connection, capacitor voltage is approx. phase voltage respectively. This implies that for equal reactive power production, capacitances must be three times larger if capacitors are connected in star, i.e. $3C_\Delta = C_Y$.

Fixed capacitor compensation is suitable for applications where reactive power demand is somewhat constant. Amount of required fundamental frequency reactive power of the motor load at certain operating point can be calculated

$$Q_{load} = 3U_{load} I_{load} \sin(\phi) = \left(\frac{U_{load}}{U_n}\right)^2 Q_n = \frac{3U_{load}^2 I_n \sin(\phi)}{U_n} \tag{40}$$

where U_n, I_n and Q_n are nominal voltage, current and reactive power. (40) assumes that load current at certain supply voltage is directly proportional to of ratio supply voltage and nominal supply voltage.

Because output supply voltage is controlled using scalar control, ratio of supply voltage RMS and supply voltage frequency is kept constant, i.e. $\frac{U}{f} = k$. When this ratio is adapted to (39), absolute value of the fundamental reactive power produced by capacitor bank can be re-formulated

$$Q_c = \frac{6\pi}{k} U_c^3 C \tag{41}$$

As (41) implies, produced reactive power is a 3rd order function of operating frequency and (40) shows that reactive power of the load is proportional to the square of motor voltage.

It is evident that at some frequency, produced reactive power becomes larger than reactive power drawn by load. This condition can be called overcompensation. Overcompensation is undesired because if reactive power is produced more than drawn by the load, additional capacitive current is injected to system. This increases power losses and can for example cause overvoltages to motor terminals. Operating point where overcompensation region begins can be calculated combining (40) and (41). Overcompensation occurs if

$$f > \frac{1}{6\pi C}\frac{Q_n}{U_n^2} \tag{42}$$

(42) is valid, if same voltage affects over both motor coils and capacitors i.e. motor and capacitors are both connected either in delta or in star connection.

To investigate a frequency where overcompensation occurs, reactive powers were calculated as a function of operating frequency. Capacitor reactive power was calculated using (41) and for simplicity, scalar control ratio from frequency to output line voltage was kept constant value of 4.2 over whole frequency range. In reality, power factor of the motor doesn't remain constant over frequency range. Generally, the closer operating point is to nominal, the larger is power factor. Load reactive power demand was calculated with different constant power factors using (40). Calculations were carried out for larger frequency range than actual relevant range to find out theoretical limit of overcompensation. Calculation results are shown in Figure 26.

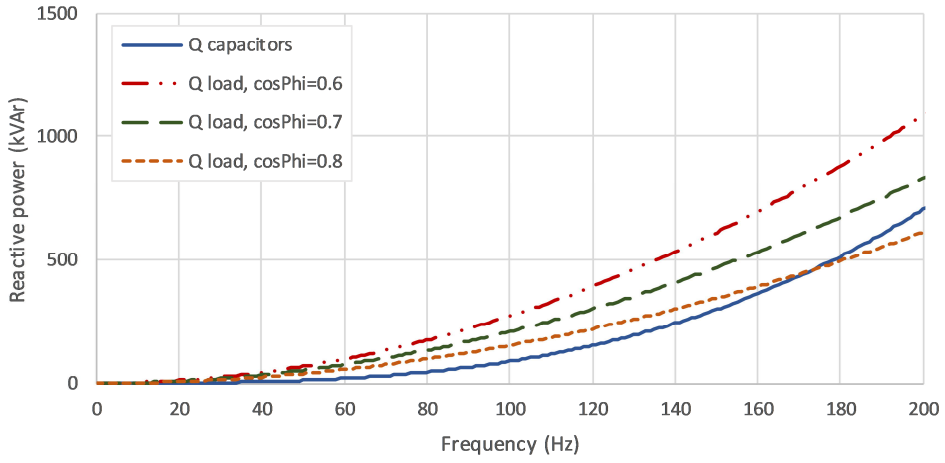

Figure 26. *Supplied and required reactive power at different load power factors.*

When load power factor is kept constant, overcompensation occurs at lower frequencies. As seen from results in Figure 26, overcompensation occurs at 170 Hz when power factor

is kept at 0.8. At lower power factors overcompensation limit frequency is higher than 200 Hz.

Analysis above is based on multiple simplifications and overcompensation limit results are not accurate. Only fundamental frequency is considered, and harmonics are left out. Also, all other effects such as power cables and parasitic components are neglected. In reality, motor power factor doesn't remain constant but even at nominal load power, power factor is less than 0.8. Real scalar control ratio doesn't remain constant near nominal frequency and real voltage is lower compared to ideally calculated voltage. Despite the simplifications, analysis shows that for filter used in FAT-setup overcompensation doesn't occur at frequencies 170 Hz or below if the filter is working properly.

Calculation results above also show again that reactive power produced by filter capacitors is negligible at low frequencies and difference between produced and demanded reactive power is largest at frequencies around 100 Hz. This matches filter loss results and analysis in Chapter 4.5. Largest difference between produced and demanded reactive power implies largest current with largest harmonic content. That again implies largest filter losses.

Based on voltage measurements, fundamental frequency reactive power produced by the filter capacitors were calculated at different frequencies. Reactive power and fundamental output line voltage as a function of operating frequency are shown in Figure 27. In delta-connection, line voltage is equal to capacitor voltage.

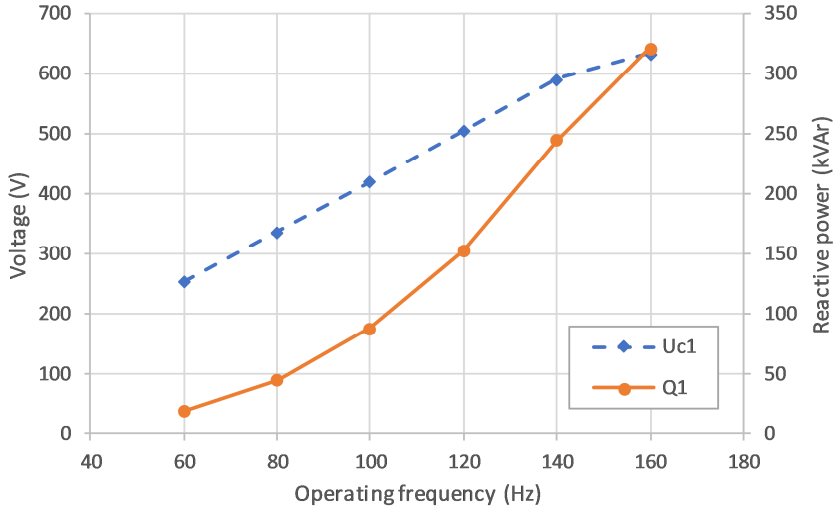

Figure 27. *Fundamental capacitor reactive power and output voltage.*

Reactive power in Figure 27 follows the waveforms in Figure 26 up to 140 Hz and voltage increases linearly. Beyond that, voltage doesn't increase linearly due to overmodulation. As a result, produced reactive power doesn't follow the exact form of (41). At frequencies near nominal, produced reactive power waveform increases slower than at lower frequencies.

Calculated and measured results above show, how filter dimensioning and operating frequency are critical in fixed capacitor compensation. At low frequencies compensation is negligible which increases reactive power drawn from supply. This can be seen as higher supply current. Higher current demand might cause problems for example if VFD current limits are set according to nominal operating point. Maximum current demand cannot be evaluated based on nominal operation. Instead, filter compensation effects must be taken into account.

5. MOTOR SUPPLY AND TERMINAL VOLTAGE

5.1 Motor supply cables

Depending on application and customer's needs, all kinds of supply cable configurations have been used in the paper industry with the EP-turbos. In addition to multi conductor cables, multiple single conductors have been used. However, cable configuration does matter, and cables cannot be chosen only based on the cross-sectional area. In VFD applications mutual effects between conductors must also be considered. Different supply cable configurations for EP-turbos are considered in this chapter. Purpose is to produce useful information for different vacuum system projects.

5.1.1 Multi-conductor cable configurations

Generally, three-phase motor power supply is implemented by three-conductor power cables or by single conductors. Three-conductor cables are electrically symmetrical, because all conductors are so called active conductors i.e. all conductors carry three-phase current. Schematic of a symmetric three-conductor cable with conductive overall shield is shown in Figure 28. This kind of cable structure is the most recommended for turbo blower applications.

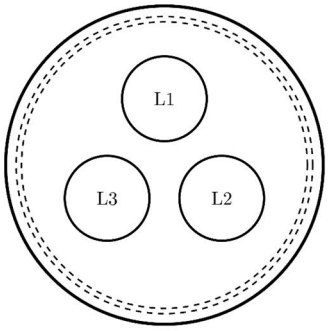

Figure 28. *Symmetric three-conductor cable with conductive shield.*

Other common cable configuration is four-conductor cable, which is asymmetric due to the fourth non-active conductor. However, this kind of cables are widely available and very often quite cheap, which could tempt to use them as VFD output cables. Examples of asymmetric four-conductor cables are shown in Figure 29.

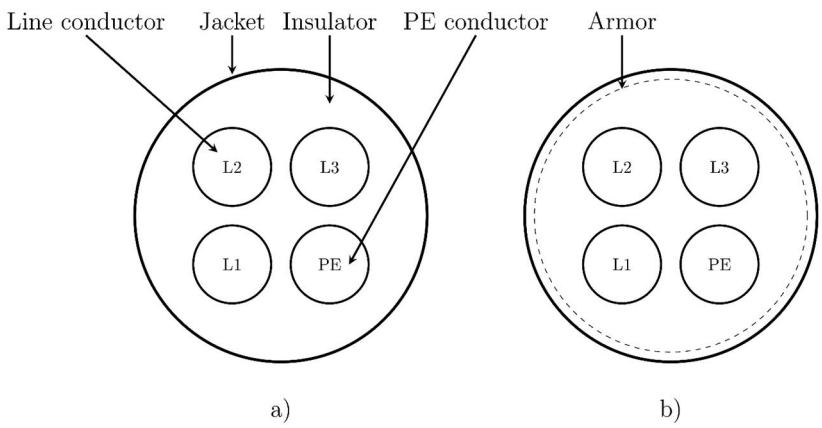

Figure 29. *Asymmetric four-conductor cables: a) Without armor b) With armor. Based on [28].*

According to variable frequency drive manufacturers, asymmetric supply cables should not be used in VFD-applications [28, p. 25]. Due to the PWM-switching waveform, frequency converter produces always some common-mode voltage to its terminals. This common-mode voltage occurs in PE-conductor and might include very fast transients. In asymmetric cable, mutual inductances between PE-conductor and each active conductor are not equal due to the cable geometry. Mutual inductance between two adjacent conductors differs from the mutual inductance between two diagonal conductors [29]. This might lead to voltage unbalance between active conductors, which again can cause errors to VFD-control system or even affect the motor performance.

PE-conductor is usually connected to VFD's ground. Voltage induced to PE-conductor due to fast common-mode voltage transients increases potential difference between motor and the ground. The phenomena described above might occur with both shielded and unshielded cables. According to [30], voltage produced between motor terminals and ground is much higher in unshielded cables. In supply systems where separate conductors are used, the fourth inactive conductor should not be located very close to active conductors asymmetrically. Otherwise same undesired phenomena might occur, even if separate conductors are used. [18, pp. 490–491]

Like the mutual inductances, capacitances between each conductor of the four-conductor cable are not equal. Capacitances are cable and frequency dependent, but capacitance between diagonal conductors can be even 7–8 times higher compared to capacitance between adjacent conductors [29]. Overall operating capacitances are somewhat higher in four-conductor cables. For example, if three- and four-conductor MCMK copper cables with cross-sectional area of 240 mm^2 and concentric shield are compared, overall operating capacitances are 0,75 $\frac{\mathrm{pF}}{\mathrm{m}}$ (three-conductor) and 0,85 $\frac{\mathrm{pF}}{\mathrm{m}}$ (four-conductor) [31].

In a case of three-conductor cable, common-mode impedance increases when cable length is increased. Common-mode current is also almost equal in both motor and inverter terminals. In four-conductor cable, increasing the cable length increases stray capacitances respect to the ground potential and common-mode impedance is decreased. This leads to higher common-mode current. Some of the common-mode current flows through the ground capacitances and therefore common-mode current in inverter terminals is larger than in motor terminals. This effect is emphasized in shielded asymmetric cables. [32] Undesired effects due to the fourth conductor get stronger while frequency or cable length are increased. Exact limit for maximum cable length can't be easily defined and it depends on power rating of the system. Therefore, cables including three active conductors and multiple PE-conductors set symmetrically around the cable midpoint should be used [28, p. 25].

Electromagnetic symmetry can be achieved by dividing inactive PE-conductor into multiple conductors and placing them symmetrically around the active conductors and the mid-point of cable cross-section. Typically, this kind of cable arrangement consists of three separate PE-conductors. Examples of different symmetrical cable configurations are shown in Figure 30.

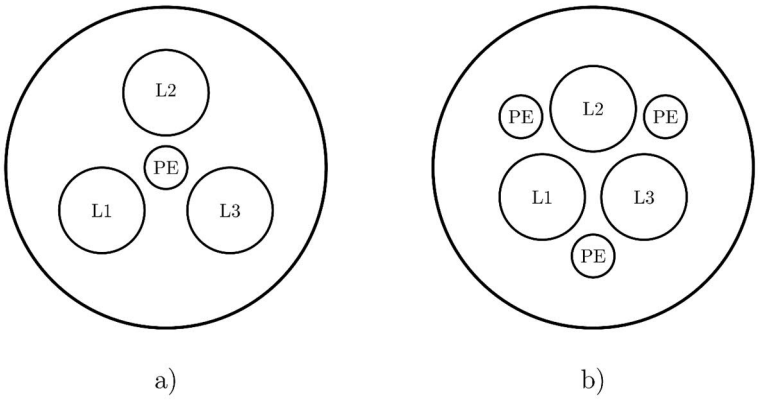

Figure 30. *Different symmetrical cable configurations: a) Single PE-conductor b) Multiple PE-conductors symmetrically. Based on [28, p. 25].*

According to measurements in [30], common-mode current in PE-conductor is much lower in cable with multiple PE-conductors placed symmetrically, compared to cable with single PE-conductor.

5.1.2 Cable shielding

In addition to conductor arrangement, cable shielding should be considered. Generally, cable with concentric shield or sheath should be preferred because it decreases cable

transfer impedance. Low transfer impedance reduces possible potential difference between motor frame and ground. [30] Shield also mitigates possible electromagnetic interference (EMI) between motor cables and other systems and strengthens the cable structure. Cable can include metallic armor instead of the shield. The armor is very similar to the shield, but its main purpose is to strengthen the cable's structure. In the shielded cables, the effective capacitance of the cable per unit length is generally higher compared to an unshielded cable. According to measurement in [33], capacity between line conductors is approx. doubled in the shielded cable compared to the equal unshielded one. For this reason, maximum cable length of an unshielded cable is longer compared to shielded cable. [28, p. 20]

On the other hand, in a shielded cable, capacitance between line conductors and its surroundings is equal everywhere along the cable. In an unshielded cable, capacitive coupling between line conductors of the cable and grounded parts of the surroundings, such as cable ladders, might occur and this coupling varies along the cable path. Electric field might be concentrated at the point where cable is in touch with grounded object and might cause some corona discharges, which again damage the insulator. If cable the insulation is somehow damaged in an unshielded cable, a small capacitive current starts to flow between the grounded cable ladder and the line conductor. This current could increase over time and cause serious damage to the cable or even to the whole power system.

In addition to asymmetric cables, shielded three-conductor cable with individual shields for each conductor are against manufacturers' recommendations [34, p. 79]. Example of this kind of cable is shown in Figure 31. This cable configuration is basically electromagnetically symmetrical, but cable shield and conductor shield form a large capacitance which causes capacitive current through the insulator. Common mode current can also be generated to individual shields and then common-mode current flows asymmetrically around line conductors. This can cause voltage asymmetry.

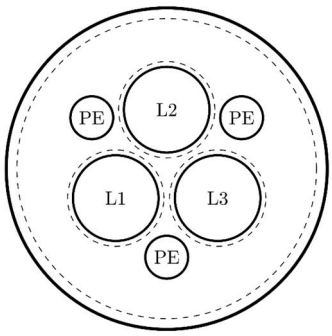

Figure 31. *Symmetric cable with individual conductor shields. Based on [34, p. 79].*

Effects due to asymmetric motor power cables could cause problems or unwanted behavior of the motor or the supply system. On the other hand, most of the effects described above are related to common-mode voltages and currents with one way or another. Use

of output sinusoidal filter at the inverter output terminals reduces common-mode effects significantly, and unwanted effects of asymmetric cables won't necessary occur. In high power applications, switching frequencies are usually relatively low. Effects of unbalanced capacitances and inductances between cables are amplified at higher frequencies, which is why those effects must be considered more carefully if higher switching frequencies are used. However, shielded three-conductor cable shown in Figure 28 is the most recommended multi conductor supply cable for EP-turbo applications.

5.2 Motor terminal voltage considerations

Stator windings of the EP-turbo motors don't include strengthened insulation due to limited space. Therefore, maximum voltage capacity of the windings is limited. In addition to the winding voltages, voltages respect to the ground potential should not become too high. There have been situations in customer applications where too high ground voltages have caused problems and undesired phenomena.

As described in chapter 3, VFD output voltage includes fast raises and falls of the voltage i.e. high absolute values of dv/dt. According to general electromagnetic theory, high frequency voltages can be analyzed as waves in some cases and applications. Just like any other electromagnetic wave, voltage transient moves along the medium at certain speed defined by electromagnetic properties of the medium [23, pp. 544–548].

Depending on the cable and load properties, voltage waves might reflect from the cable-to-load -boundary. Properties of this reflection can be characterized by cable surge impedance Z_{cable} and cable closing (boundary) impedance Z_o. Reflected voltage amplitude can be approximated as:

$$e_{ref} = \frac{Z_o - Z_{cable}}{Z_o + Z_{cable}} e_{in}, \tag{43}$$

where e_{ref} is reflected voltage amplitude in p.u. and e_{in} is incoming voltage amplitude [35]. In most motor applications, due to the motor impedance, boundary impedance is much higher than the cable surge impedance. When this is applied to (43), reflected voltage amplitude can be approximated [35]

$$e_{ref} \approx e_{in.} \tag{44}$$

Definition (44) gives upper limit to the reflected voltage amplitude and it holds completely only at the case of perfect reflection. Cable-to-load boundary behaves somewhat like a soft or an open boundary in mechanical reflection and the reflected voltage wave has same polarity with incoming wave. Because total voltage amplitude is the sum of incoming and reflected voltage waves, (44) implies that maximum short time voltage in

motor terminals due to reflection can be twice as the original incoming voltage. In practice, such high voltages won't occur due to natural damping of the cable.

Reflection described above might occur if voltage rise time is shorter than twice of the wave travel time from source to the reflection point. If wave travel speed and cable length are included, reflection might occur if

$$\frac{2l_{cable}}{v_{wave}} > t_{rise}, \tag{45}$$

where l_{cable} is length of the cable, v_{wave} is voltage travel speed and t_{rise} is supply voltage rise time [35]. Rise time is inversely proportional to the absolute dv/dt-value of supply voltage. Voltage wave traveling speed can be calculated by

$$v_{wave} = \frac{c}{\sqrt{\epsilon_r \mu_r}}, \tag{46}$$

where c is the speed of light [23, p. 547]. According to [35], voltage wave travels approximately half of the light speed. Definition (45) implies that if motor supply cables are too long compared to voltage rise time, voltage reflection may occur, and it can cause short time overvoltage to motor terminals.

Completely different origin of too high ground voltage is the use of VFD with active rectifier (AFE). There have been cases in the field where VFD has included AFE instead of a conventional passive rectifier. AFE can draw almost sinusoidal current and it has capability to produce higher DC-link voltage compared to passive rectifier. However, due to the excitation mechanism and active switching commands of the AFE, common-mode voltage respect to ground potential might vary. Use of AFE might cause repeating overvoltage more than 2000 V respect to the ground. This causes constant voltage stress to stator winding insulations. [13, 36] This phenomenon is not dependent on voltage reflection and additional voltage reflection might increase peak voltages even more. Generally, VFDs should not be used in AFE-mode in turbo blower applications to prevent undesired voltage stress.

Repeating overvoltage causes electrical stress to the stator winding insulations. Partial discharges might occur in the insulation causing insulation aging. This reduces insulation life time and might, in some circumstances, reduce the operating time of the whole motor. [37] Problem with overvoltage spikes is that they don't necessary cause problems immediately. Instead, system can work properly at first and partial discharges can cause insulation breakdown and system failure after a period of normal operation. The analysis above shows the importance of the inverter output filter. Filter doesn't only improve motor performance and efficiency but also the overall reliability and life time of the motor.

To investigate actual voltage waveforms at the motor terminals, terminal voltage measurements were carried out in FAT-setup test bunker. During measurements, smaller EP315-turbo with nominal voltage 400 V and maximum frequency 170 Hz was used. Figure 32 shows phase voltage waveform respect to turbo blower ground.

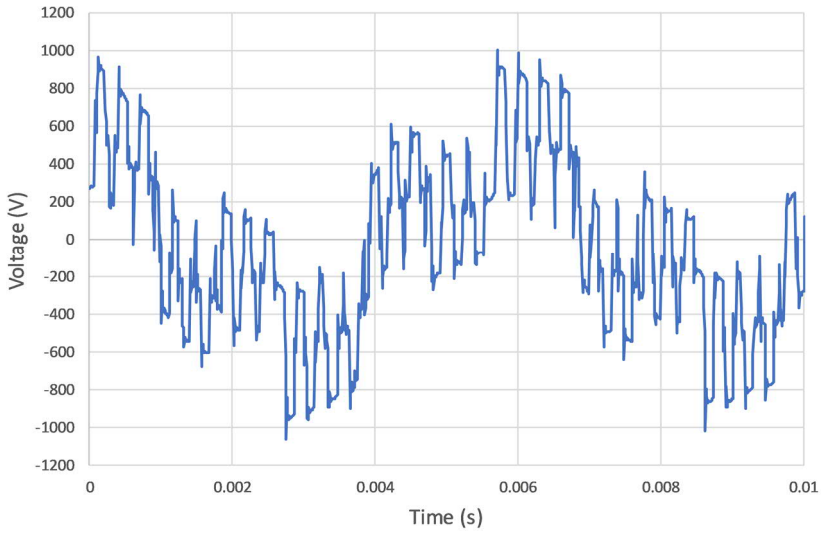

Figure 32. *EP315 terminal phase voltage respect to ground.*

As seen from Figure 32, terminal voltage contains large and short voltage spikes respect to ground. Highest voltage spikes are approx. 1000 V, which is approx. three times higher compared to the nominal phase voltage peak value. This kind of voltage spikes don't cause too much voltage stress to stator insulations, but voltage spikes of 1000 V at 400 V supply and passive rectifier imply that spikes at 690 V and AFE-drive could be intolerably high. Therefore, drives with active front-ends should not be used.

Measured line-to-line terminal voltage of EP315 at 170 Hz is shown in Figure 33. Voltage contains some additional ripple and peak voltage is approx. 580 V.

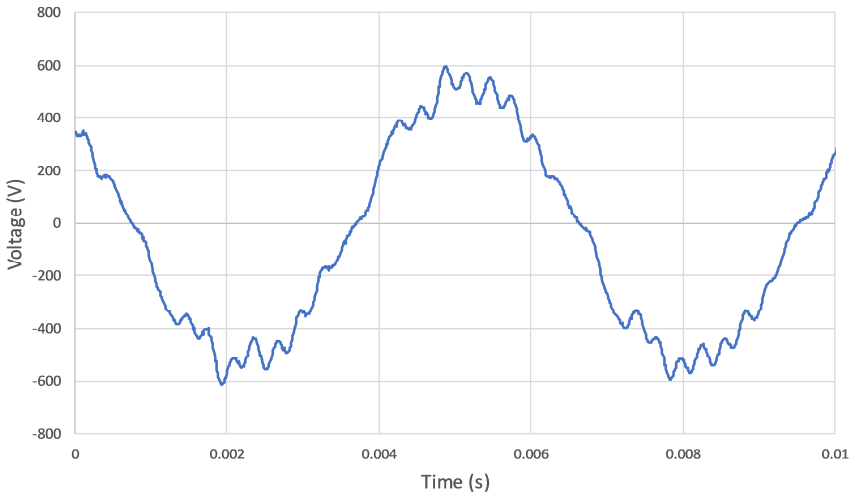

Figure 33. *EP315 line-to-line terminal voltage.*

Terminal line voltage THD up to 50 kHz was 14.2 %. Value is slightly larger compared to measurements from filter output in Chapter 4.2. At filter output measurements different turbo blower and voltage level where used and therefore THD values are not fully comparable. Power cables in FAT-setup are short, but small voltage reflections might still occur causing additional harmonics to the terminal voltage compared to the filter output voltage. Reflection spikes are naturally damped and don't occur in filter output voltages. This implies that even short supply cables have an effect on supply voltage quality.

6. CONCLUSION

Purpose of this thesis was to investigate power losses and harmonic content of currents and voltages in different segments of Runtech System's EcoPump turbo blower supply system. Main goal was to produce useful information about harmonic phenomena in different parts of the supply system. Analysis was based on Runtech's FAT-system in Kotka, Finland and all the measurements were carried out there. Especially harmonic content due to high rotational speed and low switching frequency were under interest. From the power loss perspective, output sinusoidal filter was considered carefully, because it is essential for proper operation of the high-speed turbo blower. Especially the operation of a solid rotor induction motor is dependent on output filter. In addition to power losses and harmonics, physical structure and corresponding phenomena, such as power cable configurations and effects on supply transformer were considered.

Supply voltages and currents of the VFD system were measured a under nominal turbo blower load. Due to a high input power and highly distorted input current of the six-pulse rectifier, secondary voltage of the supply autotransformer was distorted. Phase voltage THD up to 40^{th} harmonic was more than 8 %. If other devices or other turbo blowers are connected to the same supply point or a supply transformer, effects of the voltage distortion should be taken into account.

In addition to the input quantities, VFD output voltages were investigated. According to analytical consideration, VFD modulation scheme produces significant voltage harmonics around modulation frequency and its multiples. At nominal operating speed, frequency modulation ratio is small, and some base-band harmonics occur at first modulation side-band. This causes voltage harmonics from two sources to sum up causing significant harmonics at relatively high frequencies. In addition, high operating frequency causes the harmonic side-bands to be rather wide. These harmonics increase filter power losses significantly and could cause undesired resonance effects if the filter is dimensioned poorly.

Output sinusoidal filter and filter power losses were under special interest. Filter mitigates output voltage harmonics significantly, which enables proper operation of the turbo blower. At nominal operating frequency, output filter re-shapes pulsating output voltage of VFD close to sinusoidal. Because filter power losses are highly dependent on the filter current waveform, analytical method to calculate filter power losses component-wise at different frequencies was derived. Based on the measured filter currents, filter power losses at different operating frequencies and different supply voltages were calculated. It turned out that most of the filter power losses are caused by filter current harmonics and power losses are highly frequency dependent. Only a small fraction of the filter power

losses is caused by fundamental frequency current, even though most of the supply power is transferred at the operating frequency.

Based on calculations, maximum filter power losses occur at operating frequencies around 100 Hz due to higher harmonic content of the filter current. Due to poor reactive current compensation of the sinusoidal filter at lower frequencies, more energy is concentrated on higher frequencies. According to calculations, filter power losses at 100 Hz and 690 V nominal supply voltage were 8.4 kW while total output power was 174 kW. At the same nominal supply voltage and operating frequency 160 Hz filter power losses were only about 5.9 kW at output power of 482 kW. At nominal operating frequency, harmonic content of the filter current is significantly lower and for this reason filter power losses remain lower compared to lower operating frequencies. This effect should be considered in terms of system cooling and output filter design.

In addition to power losses (ΔP_{filt}), fundamental voltage drop over filter inductance ($\Delta V_{1,rms}$) was calculated at different operating points at 690 V supply. Fundamental voltage drop increases along the switching frequency, while supply voltage and fundamental frequency filter current increases. Conclusion of the current content, calculated power losses and fundamental frequency voltage drops at different operating points at 690 V nominal supply are collected to Table 9.

Table 9. *Conclusion of filter characteristics at 690 V nominal supply.*

f (Hz)	I_{RMS1}/I_{RMS}	P_{filt}(kW)	$\Delta P_{filt.}$(kW)	$\Delta P_{filt.}/P_{filt.}$	$V_{1,ph}$(V)	$\Delta V_{1,rms}$ (V)	$\Delta V_{1,rms}/V_{1,ph}$
60	72.14 %	52.3	6.96	13.30 %	146	3.4	2.3 %
80	72.05 %	103.1	7.77	7.54 %	194	4.8	2.5 %
100	71.75 %	174.4	8.39	4.81 %	242	6.4	2.6 %
120	80.22 %	263.8	7.43	2.82 %	291	8.4	2.9 %
140	80.33 %	370.2	6.34	1.71 %	342	10.6	3.1 %
160	85.96 %	481.5	5.94	1.23 %	366	13.3	3.6 %

In addition, reactive power compensation capability of the filter was also considered. Due to used scalar control, fundamental frequency reactive power produced by filter capacitors is proportional to the cube of operating frequency. Therefore, at small frequencies filter compensates natural reactive power demand of the induction motor very poorly. Filter inductances are also dimensioned based on nominal frequency operation. This increases current harmonics and relative current demand at lower frequencies. On the other hand, according to analysis, overcompensation doesn't occur at the relevant turbo blower operating frequency range.

At end of the thesis different supply cable configurations and cable length characteristics were considered. In electromagnetic perspective, most suitable multi-conductor supply cables for EP-turbos are three-conductor cables with conductive shield and symmetrical PE-conductors. Asymmetric four-conductor cables or cables with individual conductor

shields should not be used due to unequal mutual inductances and capacitances. Those cable configurations are also against VFD manufacturers' recommendations. Use of proper output filter and supply cables extend maximum length of the power cables, but too long supply cables increase power losses and increase the risk of overvoltage spikes at motor terminals. Constant overvoltage spikes might cause stress to stator winding insulations and decrease motor system life time.

REFERENCES

[1] J. Huppunen, High-speed solid-rotor induction machine – Electromagnetic calculation and design, Lappeenranta University of Technology, Digipaino, Lappeenranta, 2004, 168 p.

[2] N. Mohan, T. Undeland, W. Robbins, Power Electronics Converters, Application and Design, 3rd ed. John Wiley & Sons, Inc., Hoboken, New Jersey, USA, 2003, 802 p.

[3] Runtech Turbo EP600, Runtech Systems, 2018, 2 p. Available: https://www.gardnerdenver.com/en/runtech/energy-and-vacuum-systems.

[4] Gardner Denver Inc. ENERGY and Vacuum systems - RunEco, Gardner Denver, Inc., web page. Available (accessed 24.09.2018): https://www.gardnerdenver.com/en/runtech/energy-and-vacuum-systems.

[5] Runtech Turbo EP315, Runtech Systems, 2018, 2 p. Available: https://www.gardnerdenver.com/en/runtech/energy-and-vacuum-systems/turbo-blowers.

[6] i3000s/i2000 Flex AC Current Probe Instruction Sheet, Fluke, Literature Number: PN 2560447, 2006, 10 p. Available: https://dam-assets.fluke.com/s3fs-public/i3000s__iseng0100.pdf.

[7] Voltage Transducer CV-3 2000, LEM, Literature Number: 97.76.69.000.0, 2017, 3 p. Available: https://www.lem.com/sites/default/files/products_datasheets/cv_3-2000.pdf.

[8] NI 9220, National Instruments, Literature Number: 378023A-02, 12 p. Available: http://www.ni.com/pdf/manuals/378023a_02.pdf.

[9] S. Bhattacharyya, E. Deprettere, R. Leupers, J. Takala, Handbook of Signal Processing Systems, Springer Science+ Business Media, New York, NY, USA, 2010, 1083 p.

[10] S. Bhattacharyya, J.F.G. Cobben, W.L. Kling, Impacts of Modifications of Standards on the Power Quality Measurement Results, Proceedings of 14th International Conference on Harmonics and Quality of Power, Bergamo, Italy, September 23–26, 2010, IEEE, Piscataway, NJ, USA, pp. 1–6.

[11] T. Pitkänen, Fast Fourier Transforms on Energy-Efficient Application-specific Processors, Tampere University of Technology. Publication 1240, 2014, 176 p. Available: http://urn.fi/URN:ISBN:978-952-15-3426-3.

[12] A.E. Emanuel, Summary of IEEE standard 1459: Definitions for the measurement of electric power quantities under sinusoidal, nonsinusoidal, balanced, or unbalanced conditions, IEEE Transactions on Industry Applications, Vol. 40, Iss. 3, 2004, pp. 869–876.

[13] T. Weidinger, B. Piepenbreier, Analysis and Modelling of Common-Mode Oscillations of Electrical Drive Systems with Active Front End and Long Motor Cables, Proceedings of the SPEEDAM 2008 International Symposium on Power Electronics, Electrical Drives, Automation and Motion, Ischia, Italy, June 11–13, 2008, IEEE, Piscataway, NJ, USA, pp. 906–911.

[14] J. Guzinski, A. Haitham, P. Strankowski, Variable Speed AC Drives with Inverter Output Filters, John Wiley & Sons, Inc., Hoboken, New Jersey, USA, 2015, 458 p.

[15] D. Rice, A Detailed Analysis of Six-Pulse Converter Harmonic Currents, IEEE Transactions on Industry Applications, Vol. 30, Iss. 2, 1994, pp. 294–304.

[16] F. Zare, H. Soltani, D. Kumar, P. Davari, H.A.M. Delpino, F. Blaabjerg, Harmonic Emissions of Three-Phase Diode Rectifiers in Distribution Networks, IEEE Access, Vol. 5, Iss. 1, 2017, pp. 2819–2833.

[17] M. Hinkkanen, J. Luomi, Induction Motor Drives Equipped with Diode Rectifier and Small DC-Link Capacitance, IEEE Transactions on Industrial Electronics, Vol. 50, Iss. 1, 2008, pp. 312–320.

[18] J. Pyrhönen, V. Hrabovcova, R.S. Semken, Electrical Machine Drives Control: An Introduction, 1st ed. John Wiley & Sons, Incorporated, Hoboken, New Jersey, USA, 2016, 527 p.

[19] D. Grahame Holmes, T.A. Lipo, Pulse Width Modulation for Power Converters: Principles and Practice, 1st ed. Wiley-IEEE Press, Piscataway, NJ, USA, 2003, 715 p.

[20] A.C. Binojkumar, B. Saritha, G. Narayanan, Experimental Comparison of Conventional and Bus-Clamping PWM Methods Based on Electrical and Acoustic Noise Spectra of Induction Motor Drives, IEEE Transactions on Industry Applications, Vol. 52, Iss. 5, 2006, pp. 4061–4073.

[21] T. Bhavsar, G. Narayanan, Harmonic Analysis of Advanced Bus-Clamping PWM Techniques, IEEE Transactions on Power Electronics, Vol. 24, Iss. 10, 2009, pp. 2347–2352.

[22] J. Huppunen, J. Pyrhönen, Filtered PWM-inverter drive for high-speed solid-rotor induction motors, Conference Record of the 2000 IEEE Industry Applications Conference. Thirty-Fifth IAS Annual Meeting and World Conference on Industrial Applications of Electrical Energy, Rome, Italy, October 8–12, 2000, IEEE, Piscataway, NJ, USA, pp. 1942–1949.

[23] M. Mansfield, C. O'Sullivan, Understanding Physics, John Wiley & Sons, Inc., West Sussex, England, 1998, 755 p.

[24] K. Iyer, Transformer Winding Losses with Round Conductors and Foil Windings for Duty-Cycle Regulated Square Waveform Followed by Winding Design and Comparison for Sinusoidal Excitation, University of Minnesota, Faculty of the Graduate School, 2013, 65 p. Available: 10.1.1.916.5488.

[25] C. Freitag, Magnetic Properties of Electrical Steel, Power Transformer Core Losses and Core Design Concepts, Karlsruher Institutes für Technologie (KIT), 2017, 153 p. Available: https://publikationen.bibliothek.kit.edu/1000066142/4047647.

[26] A. Agasthya, M.K. Kazimierczuk, Steinmetz Equation for Gapped magnetic Cores, IEEE Magnetics Letters, Vol. 7, 2016, pp. 1–4.

[27] A. Lahyani, A. Braham, A. Bouhachem, Power loss estimation of electrolytic capacitor using genetic algorithm, INTELEC, International Telecommunications Energy Conference (Proceedings), Rome, Italy, September 30–October 4, 2007, IEEE, Hoboken, New Jersey, USA, pp. 875–879.

[28] AP10: Cabling and Wiring Guidelines SINAMICS, Cranes, Siemens AG Industry Sector, Nürberg, Germany, 2012, 59 p.

[29] O. Magdun, A. Binder, C. Purcarea, A. Rocks, B. Funieru, Modeling of asymmetrical cables for an accurate calculation of common mode ground currents, 2009 IEEE Energy Conversion Congress and Exposition, San Jose, CA, USA, September 20–24, 2009, IEEE, Hoboken, New Jersey, USA, pp. 1075–1082.

[30] J.M. Bentley, P.J. Link, Evaluation of motor power cables for PWM AC drives, IEEE Transactions on Industry Applications, Vol. 33, Iss. 2, 1997, pp. 342–358.

[31] REKA Cables Inductance and capacitance for power cables 0,6/1 kV, REKA Cables Ltd., web page. Available (accessed 12.09.2018): https://www.rekacables.com/cable-facts/technical-information/inductance-and-capacitance-power-cables-061-kv.

[32] P. Xie, J. Lu, G. Chen, H. Chen, Influence of motor cable on common-mode currents in an inverter-fed motor drive system, Frontiers of Information Technology & Electronic Engineering, Vol. 19, Iss. 2, 2018, pp. 273–284.

[33] O. Sadilek, T. Lelek, J. Korinek, Interfering Influences on Electrical Cable between Frequency Converter and Electric Motor, 26th Conference Radioelektronika 2016, Košice, Slovak Republic, April 19–20, 2016, IEEE, Piscataway, NJ, USA, pp. 2016.

[34] Hardware manual, ACS880-04XT drive module packages (500 to 1200 kW), ABB, Zürich, Switzerland, 2017, 260 p.

[35] E. Persson, Transient Effects in Application of PWM Inverters to Induction Motors, IEEE Transactions on Industry Applications, Vol. 28, Iss. 5, 1992, pp. 1095–1101.

[36] T. Weidinger, Elimination of Increased Excitation of Common-Mode Oscillations in Electrical Drive Systems with Active Front End and Long Motor Cables, Proceedings of the 13th International Power Electronics and Motion Conference, Poznan, Poland, September 1–3, 2008, IEEE, Piscataway, NJ, USA, pp. 2028–2036.

[37] M. Kaufhold, H. Auinger, M. Berth, J. Speck, M. Eberhardt, Electrical Stress and Failure Mechanism of the Winding Insulation in PWM-Inverter-Fed Low-Voltage Induction Motors, IEEE Transactions on Industrial Electronics, Vol. 47, Iss. 2, 2000, pp. 396–402.

APPENDIX A: MATLAB CODE FOR FILTER LOSS CALCULATION

Simplified MATLAB-code for component-wise filter loss calculation for given three-phase current spectrum data is shown below. Due to confidentiality some details and actual parameter values are modified or are left out. Code is modular consisting main script and three separate functions. Functions are presented below main the script.

```
%% //////////    Filter loss calculation   \\\\\\\\\\ %%
%% Main script

clear all
close all
clc

% Load current data from Excel file. Data contains frequency content of
% phase currents starting from zero frequency. Column order: phase u
% amplitude, phase u phase angles, phase v amplitudes etc.
phaseCurrents=xlsread('current_data');
Iu=phaseCurrents(:,1);
phs_Iu=phaseCurrents(:,2);
Iv=phaseCurrents(:,3);
phs_Iv=phaseCurrents(:,4);
Iw=phaseCurrents(:,5);
phs_Iw=phaseCurrents(:,6);

freq_limit=7500;      % Upper frequency limit to total loss calculation.
L=length(Iu);         % Current array length

alpha=1;              % Coefficients for loss calculation
beta=1;

Vcore1=1;             % Volumes of different parts of the core (m^3)
Vcore2=1;
Vcore3=1;
rho=1;                % Core material density (kg/m^3)
Mcore1=rho*Vcore1;    % Masses of different core parts (kg)
Mcore2=rho*Vcore2;
Mcore3=Mcore1;
Mcore=Mcore1+Mcore2+Mcore3;      % Total core mass (kg)

loss_matrix=zeros(L/2-1,4);      % Pre-allocate memory for loss data.

% Loop for loss calculation at different frequencies.
x=1:L/2-1;
for y=x
    f=y-1;            % Corresponding frequency (Hz)
    iu_peak=IuP1(y);  % Peak values of currents (A)
    iv_peak=IwP1(y);
    iw_peak=IwP1(y);
    iu_a=phs_Iu(y);   % Phase angles of currents (deg)
    iv_a=phs_Iv(y);
    iw_a=phs_Iw(y);

    % Function call for flux_calculation -function, which returns peak
    % values of magnetic flux densities at different core parts.
    [Bu_peak,Bv_peak,Bw_peak]
    =flux_calculation(iu_peak,iv_peak,iw_peak,iu_a,iv_a,iw_a);
```

```
    % Function call for core_loss_calc -function,
    % which returns specific loss densities at different
    % parts of the core.
    [specific_loss1,specific_loss2,specific_loss3]
    =core_loss_calc(alpha,beta,f,Bu_peak,Bv_peak,Bw_peak);

    % Function call for winding_losses -function, which returns total
    % winding losses at certain frequency.
    windingLoss=winding_losses(iu_peak,iv_peak,iw_peak,f);

    % Store frequency to data structure.
    loss_matrix(y,1)=f;
    % Calculate average specific loss density and store to data
    % structure.
    loss_matrix(y,2)=(specific_loss1+specific_loss2+specific_loss3)/3;
    % Calculate total core loss and store to data structure.
    loss_matrix(y,3)
    =Mcore1*specific_loss1+Mcore2*specific_loss2
     +Mcore3*specific_loss3;
    % Store winding losses to data structure.
    loss_matrix(y,4)=windingLoss;
end

% Calculate sum of core losses up to limit frequency (kW).
Total_core_loss=sum(loss_matrix(2:freq_limit,3))/1000;
% Calculate sum of winding losses up to limit frequency (kW).
Total_winding_loss=sum(loss_matrix(2:freq_limit,4))/1000;
% Calculate total filter inductor losses (kW).
Total_filter_loss = Total_core_loss+Total_winding_loss;



%% /////////    Function flux_calculation   \\\\\\\\\ %%

% Parameters: Amplitudes and phase angles of instantaneous currents at
% certain frequency.
% Return values: Peak values of instantaneous magnetic flux densities
in
% different core parts.
function [Bu_peak,Bv_peak,Bw_peak]
= flux_calculation(iu_peak,iv_peak,iw_peak,iu_a,iv_a,iw_a)

n=1;                        % number of turns
mu0=4*pi*1e-7;              % permeability of free space
muR=1;                      % relative permeability
a=1;                        % core leg dimensions
b=1;
Acore=a*b;                  % cross-sectional area of core

Iu=iu_peak/sqrt(2);         % RMS-values of instantaneous currents
Iv=iv_peak/sqrt(2);
Iw=iw_peak/sqrt(2);

% Instantaneous currents as complex quantities
iu=Iu*cos(deg2rad(iu_a))+Iu*sin(deg2rad(iu_a))*1j;
iv=Iv*cos(deg2rad(iv_a))+Iv*sin(deg2rad(iv_a))*1j;
iw=Iw*cos(deg2rad(iw_a))+Iw*sin(deg2rad(iw_a))*1j;
```

```
R_ag=1;                         % Reluctances of different core elements
R_leg=1;
R_yoke=1;

% Flux calculation in matrix form
Am=[-(R_ag+R_leg+R_yoke) R-ag+R_leg+R_yoke;
    -(2*R_ag+2*R_leg+R_yoke) -(R_leg+R_ag)];
bm=[n*(iw-iu); n*(iv-iu)];
Xm=Am\bm;

phi_u=Xm(1);                    % Flux separation
phi_w=Xm(2);
phi_v=phi_u+phi_w;

B1=phi_u/Acore;                 % Flux density calculation
B2=phi_v/Acore;
B3=phi_w/Acore;
Bu_peak=sqrt(2)*abs(B1);
Bv_peak=sqrt(2)*abs(B2);
Bw_peak=sqrt(2)*abs(B3);

end


%% //////////    Function core_loss_calc   \\\\\\\\\\ %%

% Parameters: Loss calculation coefficients, frequency and peak flux
% densities at different core parts.
% Return values: specific loss densities in different core parts.
function [loss_specific1,loss_specific2,loss_specific3]
= core_loss_calc(alpha,beta,f,Bu_peak,Bv_peak,Bw_peak)

d=1;                            % Lamination thickness
rho_r=1;                        % Core resistivity and conductivity
do_r=1/rho_r;                   % Core density (kg/m^3)
rho=1;

% Coefficients for eddy current losses, hysteresis losses and excess
% losses.
A1=f/1000;
A2=(pi^2*do_r*d^2)/(6*rho)*(f/1000)^2;
A3=(f/1000)^1.5;

% Specific loss calculation in different core parts.
loss_specific1=alpha*A1*Bu_peak^2+A2*Bu_peak^2+beta*A3*Bu_peak^1.5;
loss_specific2=alpha*A1*Bv_peak^2+A2*Bv_peak^2+beta*A3*Bv_peak^1.5;
loss_specific3=alpha*A1*Bw_peak^2+A2*Bw_peak^2+beta*A3*Bw_peak^1.5;

end

%% //////////    Function winding losses   \\\\\\\\\\ %%

% Parameters: Peak values of phase currents and frequency
% Return values: Total winding losses
function [Pwinding_tot] = winding_losses(iu_peak,iv_peak,iw_peak,f)

n=1;                            % Number of turns
Rdc=1;                          % Conductor DC-resistance
d=1;                            % Foil layer thickness
```

```
rho=1;                          % Conductor resistivity
muR=1;                          % Conductor  permeability
mu0=4*pi*10^-7;
mu=muR*mu0;

Iurms=iu_peak/sqrt(2);          % Current scaling
Ivrms=iv_peak/sqrt(2);
Iwrms=iw_peak/sqrt(2);

delta=sqrt(rho/(pi*f*mu));      % Skin depth
D=d/delta;                      % Skin effect coefficient
% Skin effect AC-resistance component
Rac_skin=(sinh(2*D)+sin(2*D))/(cosh(2*D)-cos(2*D));
% Proximity effect AC-resistance component
Rac_prox=(2/3)*(n^2-1)*(sinh(D)-sin(D))/(cosh(D)+cos(D));
% AC-resistance at certain frequency
Rac=D*(Rac_skin+Rac_prox)*Rdc
% Total winding losses
Pwinding_tot=Rac*(Iurms^2+Ivrms^2+Iwrms^2);

end
```